Received: 8 April 2024 | Revised: 15 November 2024 | Accepted: 19 November 2024

DOI: 10.1002/qj.4909

Quarterly Journal of the Royal Meteorological Society RMetS

RESEARCH ARTICLE

Distinguishing north and south African Easterly Waves with a spectral method: Implication for tropical cyclogenesis from mergers in the North Atlantic

Tanguy Jonville[1,2] | **Erwan Cornillault**[3] | **Christophe Lavaysse**[4] | **Philippe Peyrillé**[3] | **Cyrille Flamant**[1]

[1]Laboratoire Atmosphères, Milieux, Observations Spatiales, CNRS-SU-UVSQ, Paris, France

[2]Ecole des Ponts, Marne la Vallée, France

[3]Centre National de Recherches Météorologiques, Université de Toulouse-Météo France–CNRS, Toulouse, France

[4]Institut des Géosciences de l'Environnement, CNRS-UGA-INRAE-IRD-Grenoble INP, Grenoble, France

Correspondence
Tanguy Jonville MD, LATMOS, Sorbonne Université, Campus Pierre et Marie Curie, 4 place Jussieu, 75252 Paris, France.
Email: tanguy.jonville@latmos.ipsl.fr

Funding information
Centre national d'études spatiales; Météo France; Institut national des sciences de l'Univers; European Space Agency, Grant/Award Number: RFP/3-16595/20/NL/FF/ab; Ministère de la Transition Ecologique et de la Cohésion des Territoires; Institut Pierre-Simon Laplace

Abstract

African Easterly Waves (AEWs) are mixed barotropic–baroclinic instabilities, propagating both north (AEW-N) and south (AEW-S) of the African Easterly Jet. They are an important component of the North Atlantic region meteorology, influencing precipitation and convection, and are primary seeds for tropical cyclones (TCs) over the North Atlantic. In this study, a novel tracking protocol is introduced based on filtering of the 700-hPa vorticity over two frequency ranges, suited for each wave track: 2.95–4.55 days (quicker propagating mode) and 4.55–6.35 days (slower propagating mode). It is applied to a 31-year reanalysis dataset, the European Centre for Medium-range Weather Forecasts (ECMWF) Fifth Reanalysis. This method effectively isolates north-track activity even amidst dominant south-track signals, enabling better identification and tracking of northward vortices. An analysis of the climatological structure of the two modes is conducted. The slower mode propagates around 24°N and transitions from 850 hPa above the continent to 700 hPa above the ocean, consistently with AEW-N characteristics. The quicker mode propagates around 15°N and is located at the African Easterly Jet level, between 700 and 600 hPa above the continent and the ocean, consistently with AEW-S characteristics. The new method allows the detection of AEW-N even when AEW-S activity dominates the 2–10 day signal, thereby enabling the detection of more AEW-S/AEW-N mergers than in previous studies. When comparing the usual 2–10 day filtering with this new method, the proportion of TCs related to AEW mergers rises from 11% to 25%. 23.4% of mergers are found to be related to TC genesis, making mergers the most efficient precursors for TC genesis in the Atlantic. TC genesis from mergers occurs more frequently on the eastern side of the basin than TC genesis from other precursors.

KEYWORDS

African Easterly Waves, hurricanes, mergers, tropical cyclones, tropical storms, wave pouch

1 | INTRODUCTION

African Easterly Waves (AEWs) are characteristic features of the West African circulation. They grow from mixed barotropic/baroclinic instabilities (Burpee, 1972; Thorncroft & Hoskins, 1994) on both sides of the African Easterly Jet (AEJ) and are related to convection and precipitation (Mekonnen *et al.*, 2006; Cornforth *et al.*, 2009), dust outbreaks (Grogan *et al.,* 2016; Bercos-Hickey *et al.,* 2017), and modulation of the West African Monsoon (WAM) circulation (Lavaysse *et al.,* 2010). Furthermore, they are associated with tropical cyclogenesis by many studies (Frank, 1970; Landsea, 1993; Russell *et al.*, 2017). According to Russell *et al.* (2017), they are responsible for up to 70% of tropical cyclogenesis in the Northern Atlantic and up to 80% of hurricane genesis. However, the relation between tropical cyclones (TCs) and AEWs is not bijective and only 17% of AEWs trigger TC genesis (Hopsch *et al.*, 2010). Therefore, gaining an understanding of the processes that lead an AEW to develop into a tropical cyclone is still an active field of research.

A first type of AEWs has been identified in the 3–6 day period range (De Felice *et al.*, 1990; Diedhiou, 1998; Wu *et al.*, 2013). These AEWs are intense and present steady activity (Diedhiou *et al.,* 2010), related to the modulation of the AEJ (Diedhiou *et al.,* 2002). They are dominant in the June–September period (JJAS: Diedhiou *et al.*, 2010) and will be the main focus of the present study. They propagate north (AEW-N) and south (AEW-S) of the AEJ. A second type has been identified by De Felice *et al.* (1990) to be characterized by periods of 6–9 days. They are mainly observed between October and May and have a weaker impact on TC genesis (Diedhiou *et al.,* 2010).

Therefore AEWs can be regrouped into three different groups.

- AEW-S have a genesis zone collocated with a zone of strong convective activity north of Sudan, and seem to stem from MCSs in that region (Janiga & Thorncroft, 2013). Their growth is dominated by barotropic processes (Thorncroft, 1995; Pytharoulis & Thorncroft, 1999). They reach a maximum in amplitude at the altitude of the AEJ (Thorncroft, 1995; Pytharoulis & Thorncroft, 1999; Mekonnen *et al.*, 2006) and have a quasi-null amplitude at the Earth's surface (Thorncroft, 1995). The vertical gradient of vorticity is balanced by the dynamical generation of a cold core at AEJ level (Jenkins,1995).
- AEW-N develop more to the west. Their genesis is related to dry convection due to the static instability of Saharan air, which can be enhanced by the wave activity on the southern flank of the jet (Pytharoulis & Thorncroft, 1999). They can also be excited by intrusion of the Harmattan (Chen, 2006). Genesis of waves on the northern track is catalysed by pre-existing low conditions in the Saharan Heat Low (Chen, 2006). Once the incipient excitation has initiated the perturbation, the growth of northern waves is due mainly to baroclinic processes (Thorncroft, 1995), leading to peak activity at 850–900 hPa over the continent (Pytharoulis & Thorncroft, 1999).
- 6–9 day waves have trajectories north of the AEJ (Diedhiou, 1998; Diedhiou *et al.,* 2002), more intense anticyclonic phases (Diedhiou *et al.,* 1999), and activity at higher altitude (Wu *et al.,* 2013). Their genesis areas are located in Libya and in the Azores (Diedhiou *et al.,* 2010). They are associated with the variance of the Subtropical Westerly Jet in the upper troposphere (Diedhiou *et al.,* 2010) and midlatitude Rossby waves (Wu *et al.,* 2013). It is important to note that the 6–9 day wave activity is distinct from the AEW-N (Wu *et al.,* 2013).

Different methods are used to track AEWs (Thorncroft & Hodges, 2001; Fink & Reiner, 2003; Berry *et al.,* 2007; Hopsch *et al.,* 2010; Bain *et al.,* 2014). The most commonly used methods in the literature track AEW activity either using a given quantity (curvature vorticity, vorticity maxima, etc.) without any filtering (Thorncroft & Hodges, 2001; Berry *et al.,* 2007; Bain *et al.,* 2014) or using a band-pass filtered quantity—relative vorticity, as in Satoh *et al.* (2013); meridional wind, as in Dunkerton *et al.* (2009); EKE, as in Russell *et al.* (2017). The thresholds for the temporal band-pass filters commonly used are chosen to select either all groups of AEWs (2–9 days: Dunkerton *et al.,* 2009; Hankes *et al.*, 2015, or 2–10 days: Russell *et al.*, 2017; Danso *et al.,* 2022) or only AEW-S and AEW-N (2–6 days: Fink & Reiner, 2003; Hopsch *et al.,* 2010; Satoh *et al.,* 2013; Dieng *et al.,* 2017, or 3–7 days: Agudelo *et al.,* 2011). In the September 2021 cases investigated by Jonville *et al.* (2024), the detection of AEW-N using those commonly used period windows was hindered by the predominance of south-track wave activity. However, each wave track was associated with a different range of frequency in phase space. Therefore, the study introduced the idea of splitting the commonly used 2–6 day AEW period into two distinct periods (2–4.4 days and 4.4–7 days) to distinguish AEW-S from AEW-N, respectively. The use of two different detection periods, one for each wave track, allowed for a more robust and efficient tracking of individual troughs and the detection of AEW-N even with dominant AEW-S activity. This difference in AEW-S and AEW-N frequency spectra is consistent with the two peaks identified by De Felice *et al.* (1990), although

the differences in the characteristics of those two peaks were not discussed further in the literature.

In the context of TC genesis, AEW-S and AEW-N behave differently. AEW-S have to undergo structural transformation in their development process. Their cold core has to warm to become compatible with the thermodynamic structure of a TC (Jenkins, 1995; Kwon & Mak, 1990) and the anomaly of vorticity has to extend to the lower layers of the atmosphere; it has been found that the activity of the wave in the lower layers (measured by eddy kinetic energy) was highly correlated with TC genesis from an AEW-S (Russell *et al.,* 2017). AEW-S can interact constructively with the WAM trough zone to develop downward in the lower troposphere (Arnault & Roux, 2010; Ocasio *et al.,* 2021) or merge with low-level vortices initiated north of the jet (Chen & Liu, 2014; Duvel, 2021). AEW-S are also more intense than AEW-N (Dieng *et al.,* 2017) and more often coupled with convective systems than their counterparts on the northern track (Agudelo *et al.,* 2011). The synoptic environment has also been found to be important (Satoh *et al.,* 2013; Brammer & Thorncroft, 2015) and is more favorable to the south of the AEJ (higher sea-surface temperature (SST) and more humid air masses). On the other hand, AEW-N have no cold core and have a strong surface signature. They also propagate in a less favorable environment (dryer conditions and colder SST) and take a longer time to reach relative humidity compatible with cyclogenesis (Chen *et al.,* 2008). Therefore, it was long believed that AEW-N were not involved in TC genesis (Thorncroft & Hodges, 2001). AEW-N and AEW-S also exhibit differences when studied within the marsupial paradigm framework introduced by Dunkerton *et al.* (2009). It is one of the promising theoretical frameworks to describe the multi-scale processes that explain how an AEW can favor TC genesis. If the wave propagates near a critical layer where its phase speed equals the wind speed of the mean flux, then a pouch develops within the wave. Air masses inside the pouch are protected from lateral intrusions of dry air, so that convection is favored, leading to both humidification of the wave pouch and invigoration of the mother wave (Dunkerton *et al.,* 2009). Several authors have found the development of the wave pouch to be a key factor in the process of TC development (Wang *et al.*, 2010; Asaadi *et al.*, 2016; Rutherford *et al.*, 2018). Asaadi et al., (2017), for instance, found that all developing AEWs were associated with a wave pouch, while only 10% of non-developing AEWs presented such a feature. However, the presence of a cyclonic critical layer is only found to the south of the AEJ (Dunkerton *et al.,* 2009), favoring genesis from AEW-S. AEW-N need to have a southward trajectory to develop a wave pouch. This reflects on the statistics of the development of TCs. Chen (2006) found that TCs related to an AEW-S are approximately 1.7 times more frequent than TCs related to an AEW-N, consistently with the trends observed by Brammer and Thorncroft (2015) and Ocasio *et al.* (2021). The efficiency of genesis from AEW-S is twice that of AEW-N (Chen *et al.,* 2008).

AEW-N and AEW-S merge frequently over the ocean after they leave the continent (Reed *et al.*, 1988; Pytharoulis and Thorncroft, 1999). This sometimes leads to an invigoration of their pre-existing vorticity centers that might contribute to the cyclogenetic process (Ross & Krishnamurti, 2007). As the two wave tracks peak at different altitudes, the merger of AEW-N and AEW-S can catalyse the vertical development of the vortex (Chen & Liu, 2014; Duvel, 2021) and result in more coherence between the low-level circulation and the jet-level circulation Wu *et al.* (2013). Regarding the marsupial paradigm framework, Wang *et al.* (2012) hypothesised that it is necessary for cyclogenesis to happen so that the pouch extends from 600 hPa to the boundary layer, and Brammer *et al.* (2018) found the vertical coherence of the vortex to be a key predictor of the efficiency of the pouch to favor convection. The development of a vertically coherent and aligned vortex associated with the merger of an AEW-N and an AEW-S deepens the AEW-S wave pouch and enhances its effects (Hankes *et al.*, 2015; Jonville *et al.*, 2024). Hankes *et al.* (2015) found that 25% of tropical cyclogenesis in the Atlantic east of 40°W was linked to the merger of an AEW-N and an AEW-S.

A first aim of the present study is to assess whether the approach proposed by Jonville *et al.* (2024) based on case studies can be generalised in a climatological sense and whether the detection of AEW-N and AEW-S in two distinct periods can be achieved over 30 years or more. To highlight the added value of the approach proposed in this study, AEWs are first tracked with the most comprehensive filter used in the literature (2–10 days) and in a domain extending as far north as 30°N (whereas most studies are bounded at 20°N) to capture all AEW activity. The wavelet power spectrum of days with active AEWs is then composited to identify the spectral characteristics of each wave track. On this basis, two new trackings are performed using the period windows associated with each wave track and the results are compared with the method using the broader pass filter.

As the band-pass filtering period bands commonly used in the literature fail to detect some AEW-N in the presence of dominant AEW-S Jonville *et al.* (2024), the importance of AEW mergers on cyclogenesis in the Atlantic may be largely underestimated. A second goal of this study is to compare the detection of mergers in the context of TC genesis when using the wide band-pass period commonly used in the literature (2–10 days) and the proposed approach based on distinct filtering for AEW-N

and AEW-S. The impact of this new method on the relationship between TCs and AEWs on the one hand and between TCs and AEW mergers on the other is discussed based on statistics conducted over a 30+ year archive.

2 | DATA AND METHODS

2.1 | Data

The data used in this article are reanalysis data from the European Centre for Medium-range Weather Forecasts (ECMWF) Fifth Reanalysis project (ERA5: Hersbach *et al.*, 2020), with a spatial resolution of 0.25° and a temporal resolution of four points per day for the months of June, July, August, and September (JJAS) between 1991 and 2021. When specified, data are filtered using a simple Fourier filter applied on three-month-long time series centered on the month of interest. When a filter is applied, zonal wavelengths are also filtered with a 2000–6600 km band-pass filter (corresponding to wavenumbers in the interval 6–20: Roundy & Frank, 2004; Kiladis *et al.,* 2006; Schreck *et al.,* 2012).

2.2 | Wavelet decomposition

As AEWs are greatly impacted by the seasonal cycle, the evolution of the spectrum in time has to be accounted for. Wavelet decompositions are computed with a complex Morlet wavelet using PyWavelet (Lee *et al.,* 2019), following the recommendation of Torrence and Compo (1998). As for the Fourier filters, the wavelet decompositions are computed on three-month time series centered on the month of interest to get rid of edge effects. Following Liu *et al.* (2007), to correct the bias in power spectra, the wavelet coefficients are squared and divided by their respective scales.

2.3 | Tracking algorithm

The tracking algorithm used in this study was first developed to follow updrafts and downdrafts in stratocumulus layers (Brient *et al.,* 2019), but it is well suited for large features like AEWs. The application of this algorithm to several tropical waves will be subject to a more thorough analysis in a future publication. In order to track AEWs over the western Sahel and the Atlantic Ocean, we mainly chose the 700-hPa filtered relative vorticity field, because the 700-hPa level is the one most commonly used in the literature, so as to capture both AEW-N and AEW-S, which are known to peak around 850 and 600–700 hPa, respectively (Hankes *et al.,* 2015). Results for 850-hPa tracking are also discussed. Even if AEWs are the primary mode of variability over West Africa, their signals can be mixed with other modes of variability (see Figure 1). Filtered data enable us to isolate signals falling in the AEW spectral domain. Therefore, the AEW tracking is performed based on wavenumber–frequency filtered anomalies in the AEW domain: wavenumber 20–6, period 2–10 days (Kiladis *et al.,* 2009), specifically excluding the mixed Rossby–gravity wave domain between the two black curves in Figure 1, as their dynamics is different from that of AEWs (Matsuno, 1966).

We then apply a mask to detect all grid points where the filtered vorticity exceeds a given intensity threshold. Then, for each point belonging to the mask, the algorithm checks which neighboring points also belong to the mask, associates them, and slices the mask into the different related sets. Each set forms an object designated by an integer, which can be tracked in time or space. The position of the feature is taken as the centroid of all the points of the objects. Finally, a second threshold on the lifespan of the objects is applied to eliminate objects that cannot be considered as AEWs (lifespan too short). The choice of intensity and lifespan thresholds is discussed in the Appendix.

In the following, we will use this algorithm following different methods:

- **2–10 day tracking**: wavenumber in the interval 6–20, period in the interval 2–10 days, to capture all types of AEW activity;
- **quick-mode tracking**: wavenumber in the interval 6–20, period in the interval 2.95–4.55 days, to capture quick-mode activity (defined in the following section);
- **slow-mode tracking**: wavenumber in the interval 6–20, period in the interval 4.55–6.35 days, to capture slow-mode activity (defined in the following section);
- **quick-mode ∪ slow-mode tracking**: applying quick-mode tracking and slow-mode tracking separately and concatenating the results.

Since the period range is narrower for quick-mode tracking and slow-mode tracking, it contains less spectral energy. To detect a comparable number of AEWs, a change of intensity threshold is needed for the tracking algorithm compared with 2–10 day tracking (see Appendix for more details). The number of waves detected by the different methods is displayed in Table 1 and put in the context of different literature values.

2.4 | Detection of phasing between AEWs at 700 and 850 hPa

To identify the phasing of AEWs detected at two different altitudes (700 and 850 hPa), we consider that two AEWs

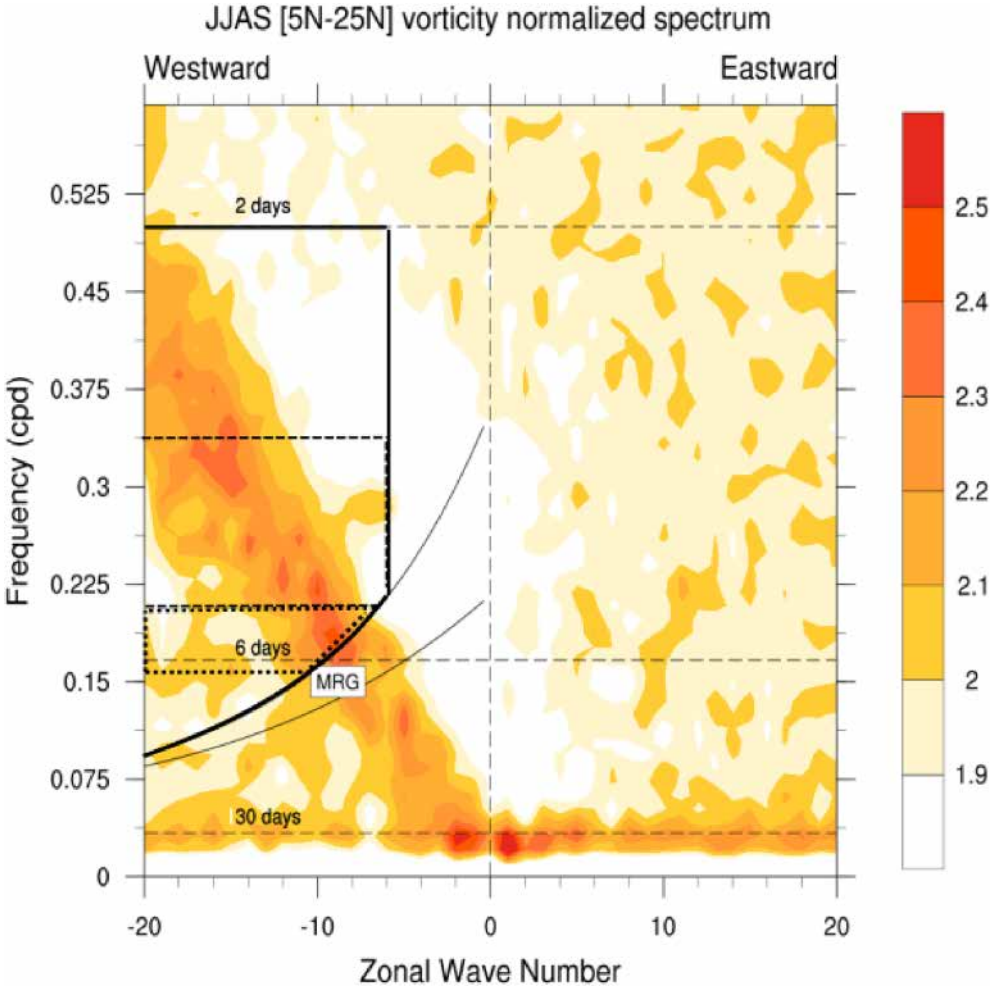

FIGURE 1 Normalized wavenumber–frequency spectrum of ERA5 700-hPa relative vorticity for JJAS 1991–2021, between 5°N and 25°N and without equatorial symmetry consideration. The bold solid polygons indicate domains for the filtering of AEW, the dashed contour the quick mode, the dotted contours the slow mode. The thin solid lines indicate the dispersion curves of MRG for equivalent depths of 12 and 90 m.

are in phase if their centers at 700 and 850 hPa are less than 3° of longitude apart.

2.5 | Detection of mergers and developing AEWs

The final aim of the present work is the study of the link between AEWs and TCs. To address this question, the AEW trajectory data are crossed with the best track dataset from the National Hurricane Center (NHC; in this section, only "named" storms—by NHC standards—are considered as TCs) found in the International Best Track Archive for Climate Stewardship (IBTrACS: Knapp *et al.*, 2010). Status and location of the TCs are given four times a day in the dataset. The database is regarded as the reference for North Atlantic TCs (Landsea and Franklin, 2013). It is considered in the following to represent the TCs in ERA5 well, as 99.5% of TCs in iBTraCS between 2000 and 2019 can also be detected in the reanalysis with an average error in the center of the system of between 50 and 60 km (Bié & de Camargo, 2023).

According to the marsupial paradigm (Dunkerton *et al.*, 2009), TC genesis is assumed to occur within the wave pouch (i.e., region of positive vorticity where the streamlines are closed in the frame of reference of the wave). That implies that an AEW contributes to the genesis process when storms develop inside the positive vorticity region, and that the center of the storm is close enough to the center of vorticity of the wave (see Figure 2). Following Duvel (2021); Hankes *et al.* (2015), if an AEW is located closer than the horizontal threshold distance to an IBTrACs system in at least one time step of their trajectories, we consider that the TC associated with the system matches the AEW. A TC is said to match a merger if it matches both an AEW-N and AEW-S according to the above criterion. Such a distance lies between two characteristic values (see Figure 2) that can be described as follows.

- R, which is an order of magnitude of the radius of a TC ($\approx$ 500 km), as a lower bound. If the AEW centroid tracked is within this distance from the TC center, the TC is inside the region of positive vorticity of the wave.
- $1/2\lambda$ (λ being the wavelength of AEW-S), which is the order of magnitude of the size of the region of positive vorticity associated with a trough ($\approx$ 1500 km), as an

TABLE 1 Characteristics of different tracking algorithms and corresponding number of AEW troughs detected. Our tracking algorithm is applied to a domain bounded to 20°N for this comparative analysis, as in most of the methods described in the literature, but the domain will be extended to 30°N in the rest of the study.

Method	Data	Years	Method	Region	Number of waves
2–10 day tracking	ERA5	1991–2021	Wavenumber–frequency filtered vorticity	60°W–50°E, 5°N–20°N 700 hPa	30.0 per JJAS
Quick-mode tracking 2.95–4.55 days	ERA5	1991–2021	Wavenumber–frequency filtered vorticity	60°W–50°E, 5°N–20°N 700 hPa	27.8 per JJAS
Slow-mode tracking 4.55–6.35 days	ERA5	1991–2021	Wavenumber–frequency filtered vorticity	60°W–50°E, 5°N–20°N 700 hPa	6.3 per JJAS
Quick-mode ∪ slow-mode tracking	ERA5	1991–2021	Wavenumber–frequency filtered vorticity	60°W–50°E, 5°N–20°N 700 hPa	34.1 per JJAS
Bain *et al.* (2014)	ERA-I	1992–2009	Maxima of curvature vorticity	5°–15°N 40°W–40°E 700 hPa	36 per JAS
Berry *et al.* (2007)	GFS	2004	Curvature vorticity	5°–20°N 20°W–30°E 700 hPa	31 per JAS
Hopsch *et al.* (2010)	ERA-40	1979–2001	Streamfunction from 2–6 day band-pass filtered wind	7°–20°N 15°W 600 hPa	26 per JAS
Fink and Reiner (2003)	ECMWF analysis	1998, 1999	Meridional wind (anomaly and 2–6 day band-pass filtered)	0°–20°N 20°W–20°E 850, 700 hPa	40 per MJJASO
Thorncroft and Hodges (2001)	ERA-I	1979–1998	Maxima of relative vorticity	5°N–15°N 5°–25°W 600 hPa	22.9–28.9 per MJJASO

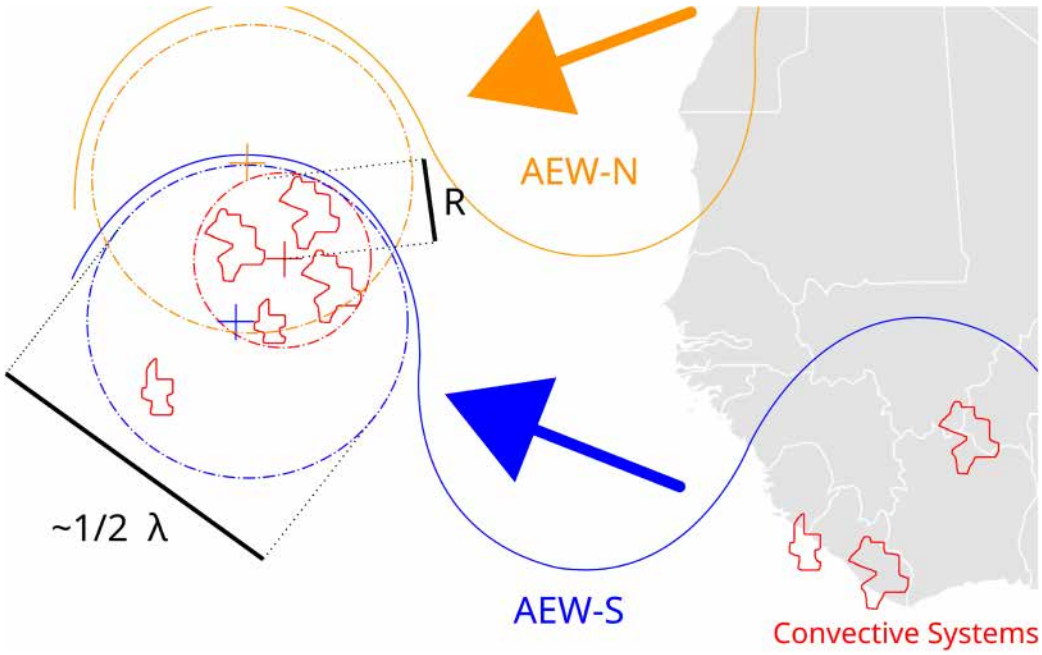

FIGURE 2 Schematic representation of potential interactions between AEWs (AEW-S, AEW-N, or both) and a TC (see text for more details). Blue and orange dashed circles represent the regions of positive vorticity of AEW-S and AEW-N, respectively. Blue and orange crosses are their centroids as tracked by our tracking algorithm. Red contours symbolise convective systems, either at mesoscale or smaller scale convective towers. The red dashed circle represents the region where the TC forms and the red cross the location of the storm center according to iBTraCS data (often the eye of the storm after the genesis). R is the average radius of a TC ($\approx$ 500 km) and λ is the wavelength of an AEW ($\approx$ 3000 km).

upper bound. The centroid is surely located within this region, and since the marsupial pouch is in the region of positive anomaly, it is the maximum value that can separate our two objects for them to interact within the framework of the marsupial paradigm.

In the following, we chose as a threshold the center of this interval (1000 km; a sensitivity analysis on the distance threshold is conducted in the Appendix). All TCs that are first detected west of 70°W cannot be matched with an AEW using this method and are therefore dropped from the dataset for the statistics presented in this study (about four named events in the Caribbean are missed per year). In the absence of a TC, mergers are detected following the same method applied to the centroids of AEW-N and AEW-S as in Hankes *et al.* (2015); Duvel (2021).

To avoid any overestimation of TC-AEW matching due to the possible double counting of some waves, a TC can be only matched once with an AEW-S, an AEW-N, or a merger. The latest occurrence in time is retained, as it is the closest in time to genesis. If an AEW-N is double-counted in the tracking dataset, it will be counted only once in the statistics regarding cyclogenesis. As for mergers that do not develop into TCs, we impose that an AEW-S can be matched with only one AEW-N so that an AEW-N counted twice would count for one in the statistics. Here, the criteria is geographic and not based on the frequency band. Again, only the latest AEW-N to merge with the AEW-S is retained, as we can make the hypothesis that it is the most likely to develop into a TC. In the case in which both the AEW-S and the AEW-N are double-counted, the merger will be counted twice, leading to a tendency to underestimate the efficiency of TC genesis from mergers. Those cases are rare, as the codetection of an AEW-S and an AEW-N close enough to allow a merger happens in both frequency bands in only 14 cases over the period under study, representing at most 5% of the total number of merger cases.

3 | RESULTS

3.1 | North and south AEW tracks at 700 hPa

Figure 3a shows the density of trajectories detected by the algorithm in JJAS 1991–2021 at 700 hPa using a 2–10 day band-pass filter. Two wave tracks appear to emerge from the density map, one to the north around 25°N, which is slightly tilted southward from east to west, and one to the south around 10°N, which is slightly tilted northward from east to west. The two tracks are clearly separated by a region of weaker wave activity located around 18.2°N above the continent. It is important to note that this latitude does not correspond to the latitude of the AEJ, observed further south (in average around 15°N; see following sections). The fact that the separation between AEW-N and AEW-S at jet level is north of the latitudinal

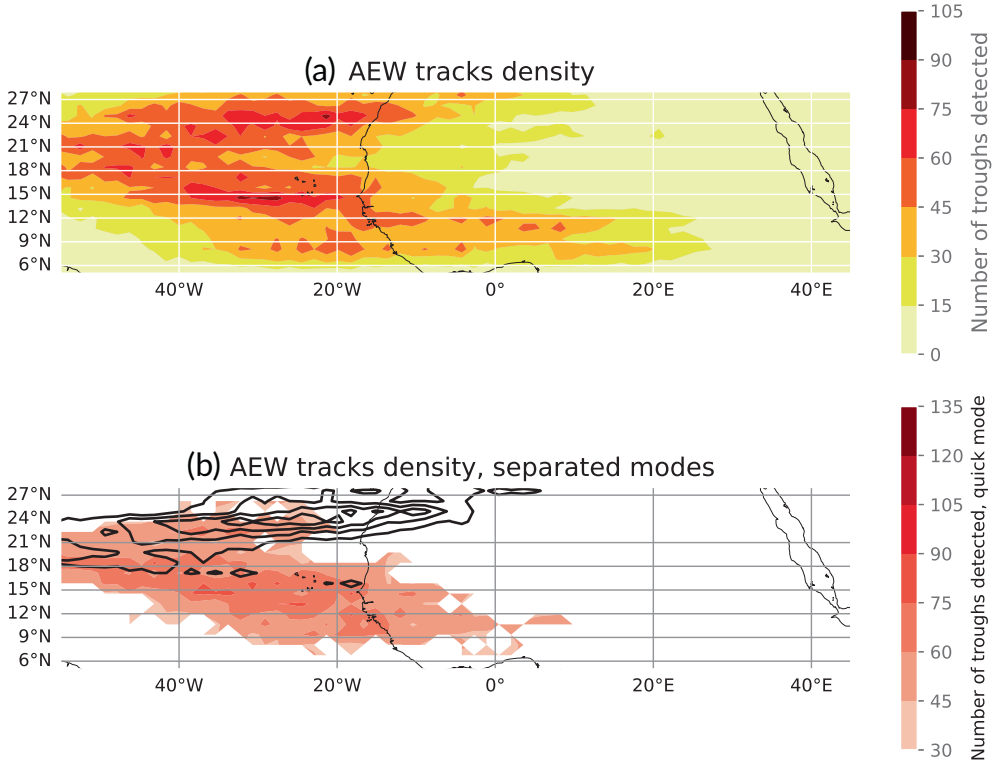

FIGURE 3 (a) Density of trajectories detected by the algorithm for the 2–10 day band-pass filter between 1991 and 2021 (JJAS). When an AEW trough is detected in a 1° by 1° grid, the count associated with this location is increased by one. (b) Same as (a), but with a band-pass filter centered on the quick mode (2.95–4.55 days, reddish colors) and slow mode (contours, from 30 troughs, a line every 15 troughs).

position of the jet itself may be explained by the fact that an easterly jet favors cyclonic cells to its south and anticyclonic cells to its north, restraining AEW-N activity close to the jet core. This region separates the two wave tracks. From 30°W and westward, the two tracks are less distinct and seem to merge west of 40°W, consistently with the findings of the literature (Duvel, 2021; Hankes *et al.*, 2015). To analyse the specific characteristics of two wave tracks, it is thus preferable to focus on the continent, where the AEJ prevents most of the mergers. Figure 4 shows the number of trajectories detected in the 2–10 day window above the continent (50°E–20°W). Two distinct peaks are observed: one at 10°N and one at 25°N, with a local minimum at 18.2°N separating the two types of AEWs.

Jonville *et al.* (2024) have shown that, in September 2021 and at 700 hPa, AEW-N and AEW-S were active in two distinct period windows: 4.4–7 days for AEW-N and 2–4.4 days for AEW-S. To investigate whether the characteristics of AEW-N and AEW-S differ over 30+ years, we composited the power spectra obtained from wavelet decompositions only on days when AEWs were active (i.e., when the algorithm detected an AEW trough), according to the following procedure. We labeled all troughs detected by the 2–10 day tracking north of 18.2°N (the longitude where the minimum in the number of AEWs detected is found, see Figures 3 and 4) as AEW-N and all troughs detected south of 18.2°N as AEW-S. We composited the power spectra at the mean latitude of AEW-N (AEW-S) on the days the AEW-N (respectively AEW-S) crossed the 20°W meridian according to our tracking algorithm. This longitude is chosen to the west of the continent where the AEJ is active and the two wave tracks are separated and where the maximum of trajectory density is reached (see Figure 3), to capture the greatest number of AEWs. Results are shown in Figure 5. The AEW-S power spectrum peaks around 3.8 days, whereas the AEW-N one peaks around 5.5 days on average in JJAS (Figure 5a). This is consistent with the findings of Jonville *et al.* (2024), who proposed two intervals for AEW-N and AEW-S in September 2021, of 2–4.4 days and 4.4–7 days for AEW-S and AEW-N, respectively. The seasonal variability (Figure 5b–e) of peak periods is not significant and the two peaks remain distinct for each month. However, the power of each peak varies significantly between June and September. The magnitude of the AEW-N peak decreases from June to

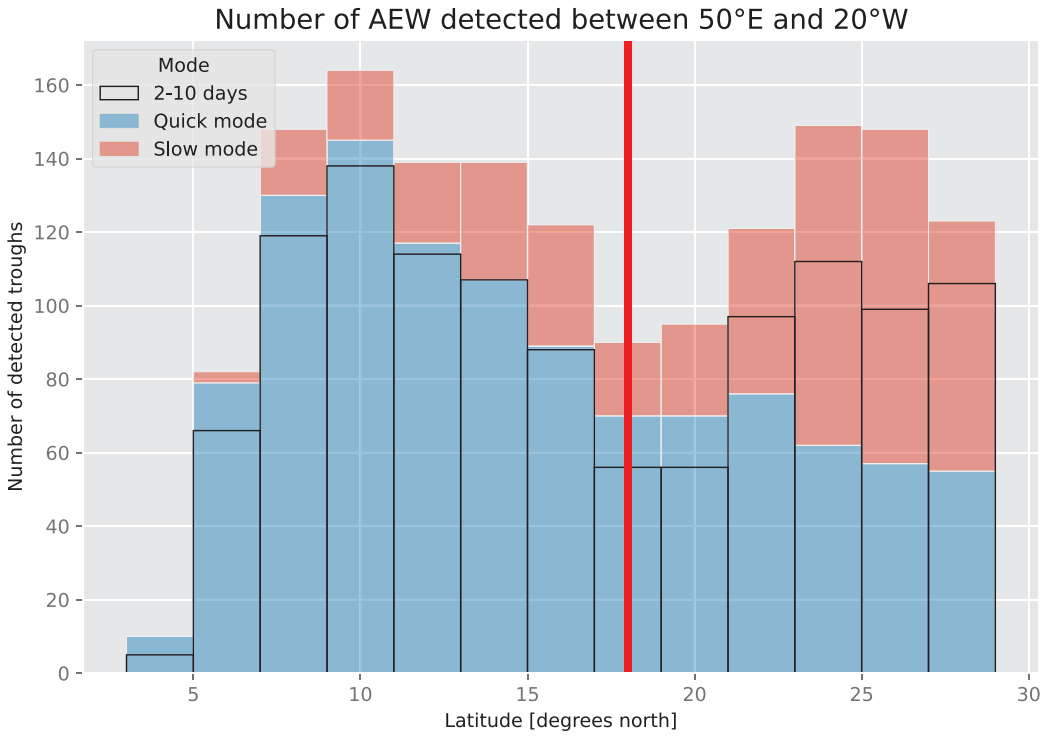

FIGURE 4 Number of objects detected by each method above the continent (between 50°E and 20°W). The red line marks the separation between AEW-N and AEW-S characterised by the minimum in the number of objects reached at 18.2°N. The dark empty boxes represent the count of detected troughs using the 2–10 day band-pass filter. The light blue boxes represent the density of detected troughs using the 2.95–4.55 day band-pass filter. The light red boxes represent the density of detected troughs using the 4.55–6.35 day band-pass filter. 2.95–4.35 day and 4.55–6.35 day band-pass filter counts are stacked to show the number of objects using the union of quick- and slow-mode tracking.

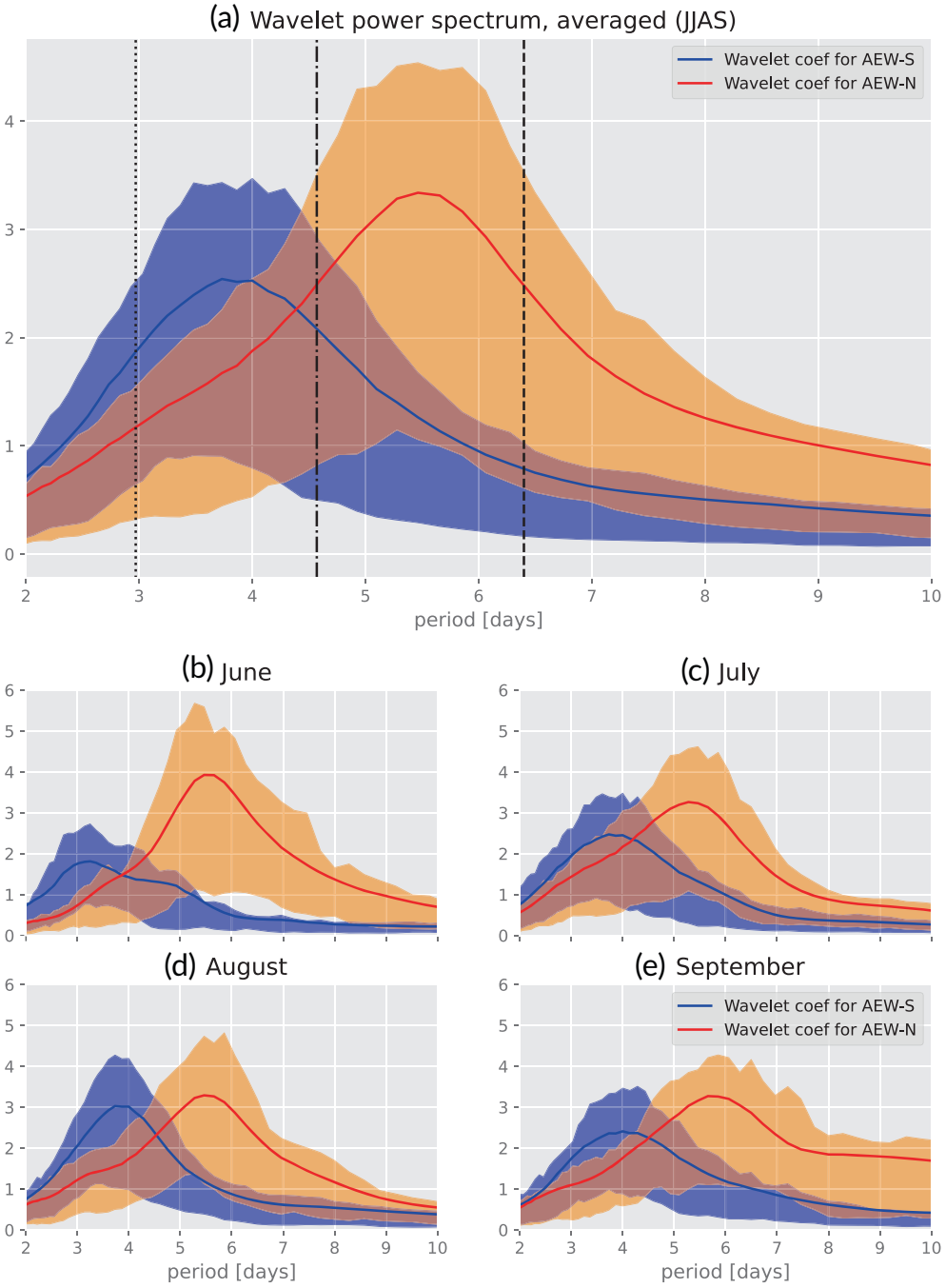

FIGURE 5 Composite of wavelet power spectrum at 20°W for AEW-N and AEW-S in (a) JJAS and (b–e) for each month from June–September. The shaded areas represent the interval between the 25th and 75th percentile.

September, whereas the magnitude of the AEW-S signal reaches a maximum in August. These results are in good agreement with the literature. Duvel (2021) shows, for instance, that vortices from the north track are more numerous in July, while the number of vortices from the south track peaks in August–September. We note that there is no peak in the power spectrum between 7 and 10 days in the period window of 6–9 day waves in June, July, and August. The only significant activity in this period range is observed in September, in accordance with the analysis of Diedhiou *et al.* (2010) on 6–9 day wave seasonality.

3.2 | Tracking at 850 hPa

AEW-N are usually tracked at 850 hPa in the literature. Figure 6 shows the results of our tracking algorithm at 850 hPa. Two groups of trajectories can be distinguished. The first one, between 5°W and 50°W and between 9°N and 12°N, appears to extend the 700-hPa AEW south track above the ocean. The second group peaks above the continent, between 10°E and 30°W and between 15°N and 19°N. It peaks just between the AEW-N and AEW-S tracks at 700 hPa and fades quickly above the ocean.

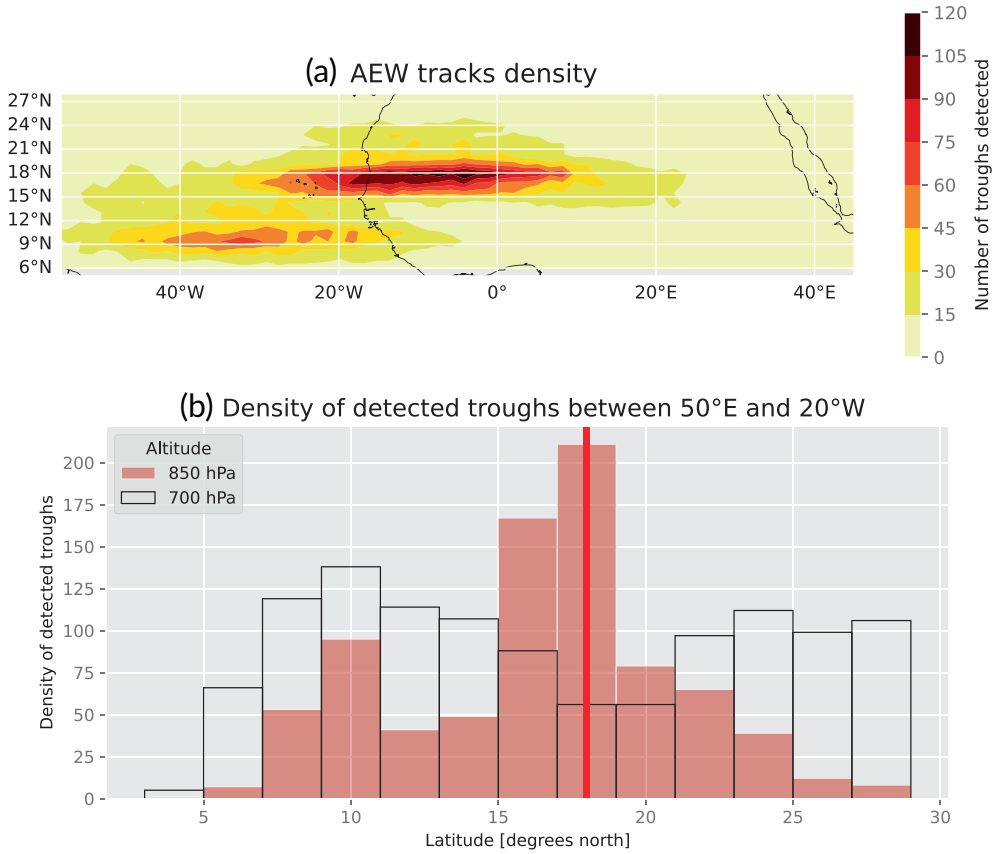

FIGURE 6 (a) Same as Figure 3 but at 850 hPa (2–10 day tracking). (b) Same as Figure 4 but at 850 hPa (2–10 day tracking).

The phasing between 850-hPa and 700-hPa AEWs is investigated to see whether the signal detected at 850 hPa in the second group of trajectories can be used to track AEW-N as has been done in the literature. 34% of the trajectories of the second group are in phase with an AEW-S at 700 hPa, 31% are in phase with an AEW-N at 700 hPa, and 35% show no match with an AEW detected at 700 hPa. When detected in phase at one time step, AEWs detected at 850 hPa and 700 hPa remain in phase for relatively long periods of time: 2.62 days on average when in phase with an AEW-N and 3.16 days on average when in phase with an AEW-S, almost a full period.

Figure 7 shows composites of 2–10 day filtered relative vorticity at 20°W for trajectories detected at 850 hPa in phase with AEW-S at 700 hPa (Figure 7a), AEW-N at 700 hPa (Figure 7b), or no AEW at 700 hPa (Figure 7c). Trajectories matching AEW-S (Figure 7a) show a stucture tilted equatorwards. The center of the circulation at 850 hPa is around 17.5°N and that at 700 hPa is located at 14.75°N. The whole column is coherent and the relative vorticity decreases only from 650 hPa. Trajectories matching an AEW-N (Figure 7b) show a strong tilt poleward, with a center of activity at 17.7°N at 850 hPa and at 21.7°N at 700 hPa. The structure is more baroclinic than for trajectories matching AEW-S and widens with altitude. It is less intense and the relative vorticity decreases from 800 hPa. The trajectories that are in phase with no AEW detected at 700 hPa (Figure 7c) show strong similarities with trajectories matching AEW-N, but with weaker dynamics and a quicker decrease in relative vorticity with altitude. One would expect that they are less prone to participate in cyclogenesis, as the intensity is one of the criteria to distinguish between developing and non-developing AEWs (Arnault & Roux, 2011). However, those unmatched waves still present a positive anomaly of relative vorticity at 700 hPa that we hope to detect using a better method.

Based on those results, the detection of an AEW around 18°N at 850 hPa is not sufficient to determine whether a trajectory is associated with north-track dynamics or south-track dynamics, as it can be associated with both. Moreover, tracking at 850 hPa also fails to follow AEWs over the ocean, where they are of interest in the context of cyclogenesis. As all types of AEWs detected at 850 hPa present a signature at 700 hPa, there is a strong interest in the use of tracking at 700-hPa level even for AEWs that used to be tracked at 850 hPa in the literature, as it allows for robust attribution of the wave track by the study of only one level. However, the weakest AEWs-N detected at 850 hPa (Figure 7c) are not detected using a 2–10 day tracking at 700 hPa. The aim of the next sections is to present a method to track AEW-N better at 700 hPa.

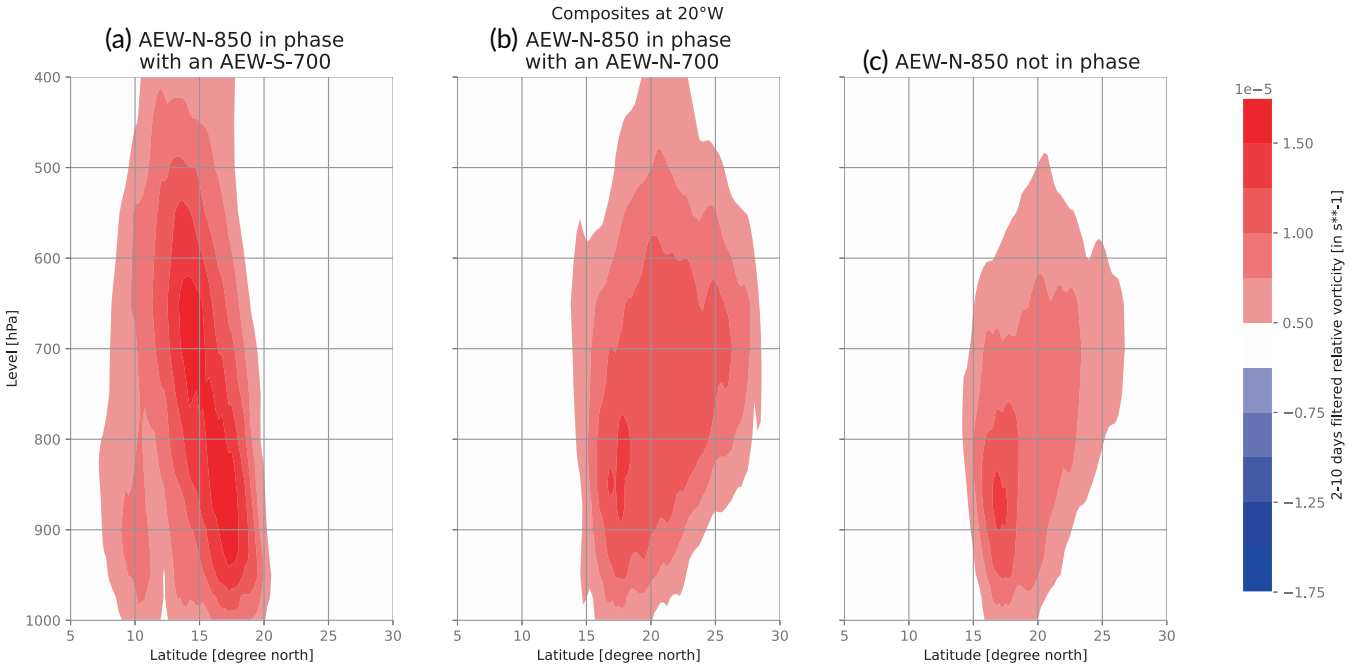

FIGURE 7 2–10 day filtered relative vorticity composited at dates on which a trajectory detected at 850 hPa reaches 20°W for AEW-850, matching (a) an AEW-S-700, (b) an AEW-N-700, or (c) no AEW-850.

3.3 | Spectral method and validation on 2021 cases

From the difference in peak period between AEW-N and AEW-S at 700 hPa, two new band-pass filtering windows are defined for the climatological period 1991–2021 (see Figure 5a): 2.95–4.55 days for AEW-S (quick-mode tracking) and 4.55–6.35 days for AEW-N (slow-mode tracking). A new tracking process is then performed on each mode. The trajectory density of each mode shows that both modes are specific to their target wave tracks (see Figure 3b). Based on the new trajectories, we can compute the phase speed for each mode and the corresponding wavelength (using the central frequency of each window as the mode frequency). Waves in the 2.95–4.55 day mode have a mean phase speed of 8.2 $m \cdot s^{-1}$ (standard deviation 1.2 $m \cdot s^{-1}$), equivalent to a wavelength of 2700 km. Waves in the 4.55–6.35 day mode have a mean phase speed of 5.8 $m \cdot s^{-1}$ (standard deviation 0.7 $m \cdot s^{-1}$), equivalent to a wavelength of 2800 km. In the following, the 2.95–4.55 day mode will be referred to as the quick mode and the 4.55–6.35 day mode as the slow mode.

Jonville *et al.* (2024) documented the fact that waves on the north track in September 2021 were not identifiable when filtering the vorticity over the period range 2–10 days. The distinction between the two modes was necessary to identify north-track activity. The three cases studied in this previous article were those observed during the Cloud–Atmospheric Dynamics–Dust Interaction in West Africa (CADDIWA) campaign (Flamant *et al.*, 2024): *Pierre-Henri* was an AEW trough associated with convection that collapsed before reaching Cabo Verde and the tropical storm stage, whereas *Peter* and *Rose* are named tropical storms. *Rose*, *Peter*, and *Pierre-Henri* were mainly associated with AEW-S, though an AEW-N event was observed in association with *Rose* and a single AEW-N event was observed in association with both *Pierre-Henri* and *Peter*. In Jonville *et al.* (2024), the waves associated with those systems were tracked manually based on the maximum of filtered relative vorticity at 700 hPa.

In Figure 8, manual tracking trajectories from Jonville *et al.* (2024) and automated tracking trajectory for each mode using the climatological band-pass periods for the quick and slow modes are compared and superimposed on the corresponding 700-hPa filtered vorticity Hovmöllers (Figure 8a, 2–10 day filter; Figure 8b, quick-mode filter; Figure 8c, slow-mode filter). The trajectories detected by our algorithm are in good agreement with the extreme values of filtered vorticity in the corresponding mode. When using the 2–10 day band-pass filtering, the automated tracking only finds three trajectories instead of the five that were tracked manually in September 2021 by Jonville *et al.* (2024). When differentiating quick and slow modes, the algorithm manages to identify five trajectories (two to the north and three to the south), in good agreement with the manual tracking performed in Jonville *et al.* (2024). The trajectories are shown in Figure 9. The

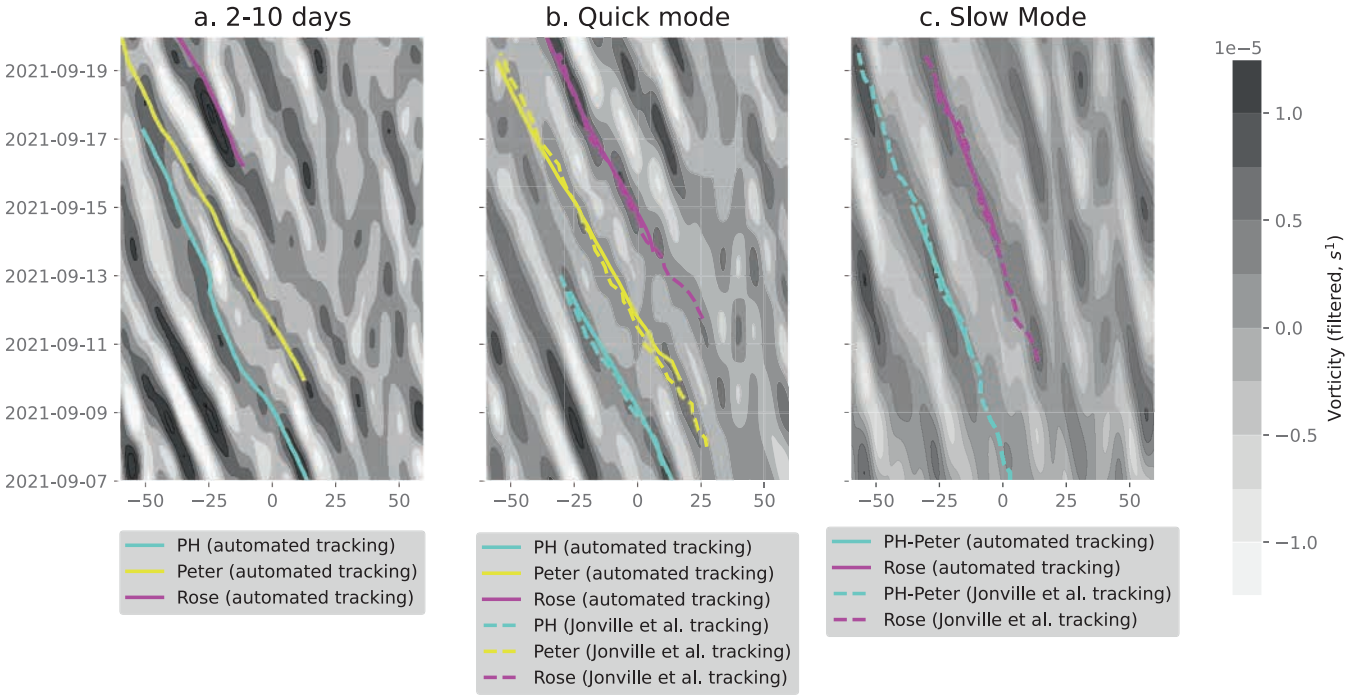

FIGURE 8 Hovmöller diagrams of filtered vorticity at 700 hPa between 5°N and 25°N and wave trajectories detected by our tracking algorithm (automated tracking) and manual trackings from Jonville *et al.* (2024). (a) Automated tracking applied to the detection of the trajectories of three of the main cyclonic features observed during September 2021: *Pierre-Henri* (PH, light blue), *Peter* (yellow), and *Rose* (pink) using the automated tracking with a 2–10 day band-pass filter. (b) Automated (solid lines) and manual (dashed lines) tracking for the same three features, but using a band-pass filter centered on the detection of the south/quick AEW mode. (c) Same as (b), but for the north/slow AEW mode and for *Peter* and *Rose* only. A single AEW-N interacted with the AEW-S associated with *Pierre-Henri* and *Peter*, hence the notation PH–Peter.

trajectories tracked with a 2–10 day band-pass period seem mostly to be attributed to the AEW-S signal, remaining mostly south of 15°N. This is consistent with the observation made by Jonville *et al.* (2024) that the wave track south of the AEJ dominates the AEW-N signal in September 2021. For *Pierre-Henri*, the trajectory in the 2–10 day mode displays a strong discontinuity around 25°W, the trajectory jumping from 17°N to 20°N, as if the automated tracking switched from a trough on the south track to a trough on the north track. On the other hand, automated trackings on the separated quick and slow modes are in good agreement with the manual trackings of Jonville *et al.* (2024). The automated tracking trajectories are slightly to the north of manual tracking trajectories for the AEW-S associated with *Pierre-Henri* and *Peter* and to the south for the AEW-S associated with *Rose*. The discrepancies in the trajectories can be explained by the difference in the method employed: whereas in Jonville *et al.* (2024), the tracking pointed at the vorticity maximum, here the centroid of all points above the threshold is retained. Therefore, the distinction between quick and slow modes in the tracking procedure not only allows us to highlight the specific structures of AEW-S and AEW-N but also allows the detection of AEW-N that were not detectable otherwise, because the signal was dominated by south-track activity when using the 2–10 day band-pass filtering.

3.4 | Structure of each wave mode

The number of trajectories detected above the continent (50°E–20°W) is displayed for each of the new band-pass frequency windows in Figure 4. The number of detected AEWs in the quick mode peaks at 10°N and decreases poleward. It detects 3% more AEW-S than the 2–10 day tracking, and 40% less AEW-N. On the other hand, the number of AEWs detected in the slow-mode trajectory increases with latitude until it reaches its peak at 25°N. It detects 82% less AEW-S and 38% less AEW-N than the 2–10 day tracking. The sum of the quick- and slow-mode track density displays similar features to 2–10 day filtering, with a minimum at 18.3°N. The number of AEW-S detected when summing quick and slow modes is larger by 18% than with the 2–10 day tracking, and the number of AEW-N is greater by 25%. As expected, the union of quick and slow mode increases, in proportion, the number

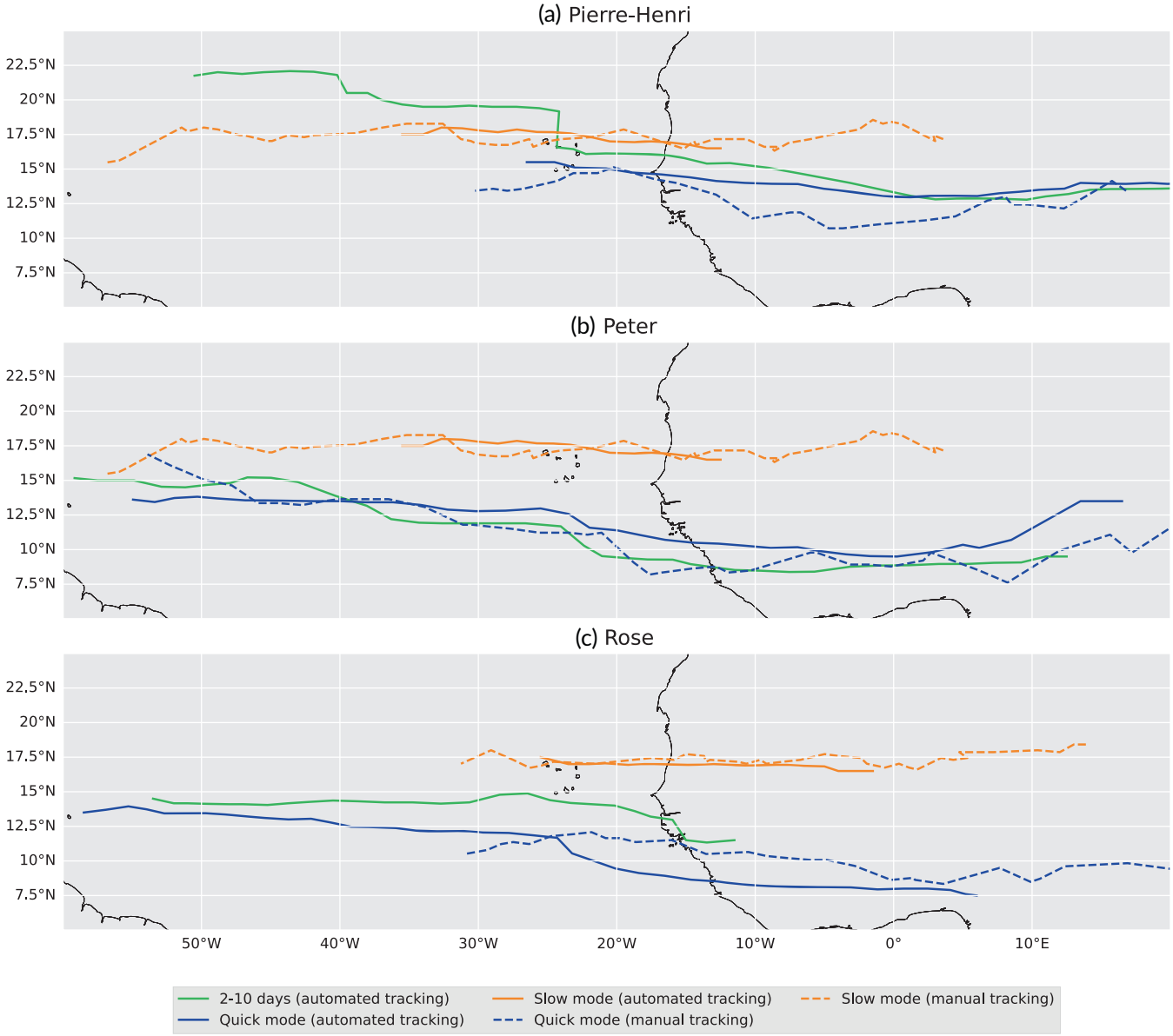

FIGURE 9 Comparison of trajectories derived from the automated tracking presented in this study using three band-pass filters (2–10 days, slow mode, and quick mode) and Jonville *et al.* (2024). Trajectories derived from the manual track appear as dashed lines, whereas ones derived from the automated tracking appear as solid lines. The trajectories derived with the 2–10 day band-pass filter are green. The trajectories associated with the quick and slow modes are in blue and orange, respectively.

of AEW-N more than the number of AEW-S. The activity of AEW-N seems split between the quick and slow modes, while AEW-S are detected in the quick mode with a wide majority. The aim of the procedure is to allow the detection of an AEW-S (respectively AEW-N) when an AEW-N (respectively AEW-S) dominates the signal, so a slight increase in the number of trajectories compared with 2–10 day filtering was expected. Despite the fact that the union of quick and slow modes might double-count some AEWs that could be detected in both frequency bands, the union of quick and slow modes does improve AEW-N detection. When using 2–10 day filtering, about 30% of the trajectories detected at 850 hPa are undetected at 700 hPa. They were associated with weaker relative vorticity. Using our new procedure, a third of those missed systems were detected as AEW-N at 700 hPa. This shows that the union of quick and slow modes improves the detection of AEW-N at 700 hPa compared with 2–10 day tracking.

The horizontal structure of each mode is analysed by compositing vorticity and wind fields (Figure 10) for slow-mode tracks (Figure 10d–f) and quick-mode tracks (Figure 10a–c). The relevance of the separation into two modes is confirmed by the structural difference between

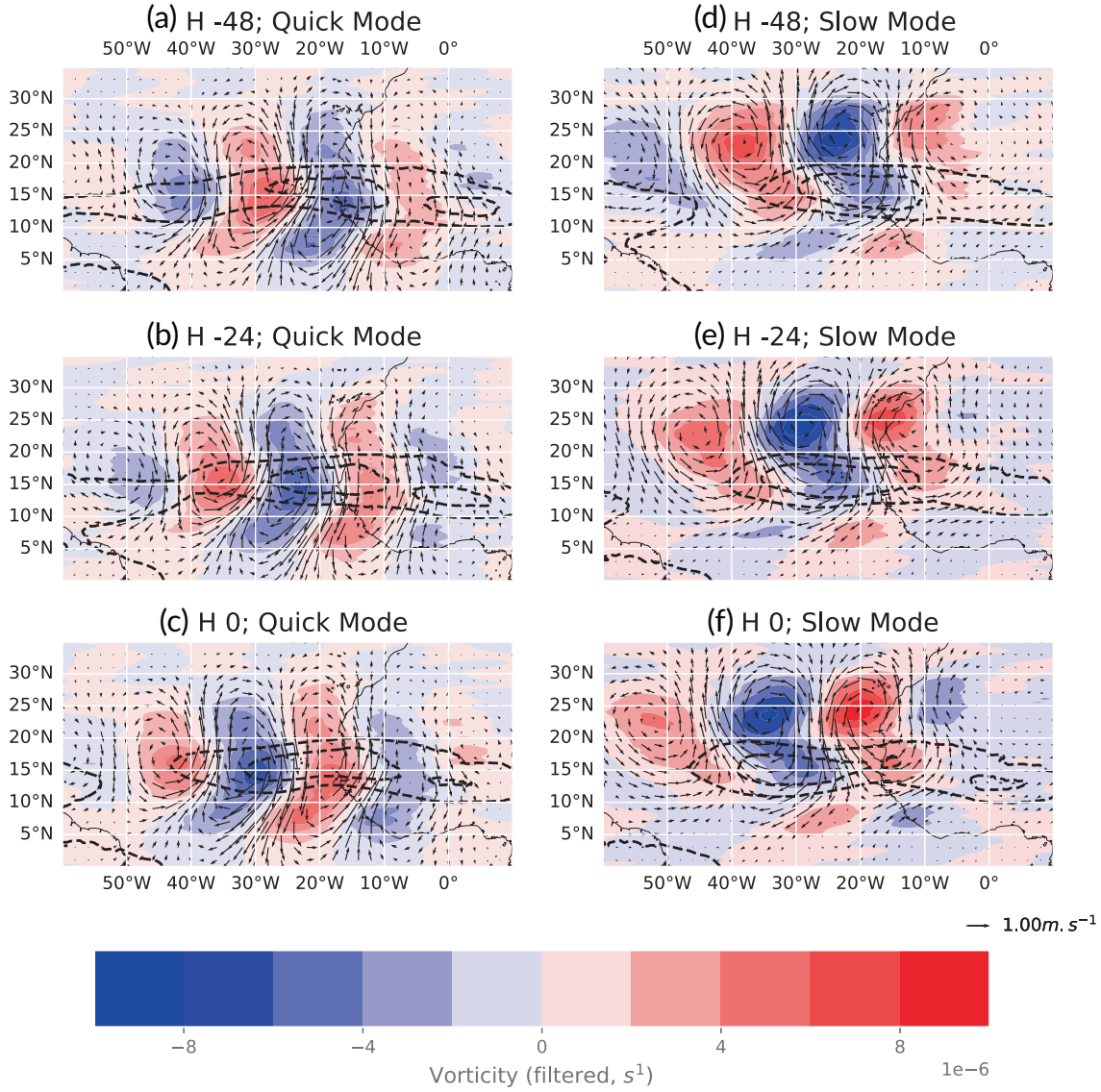

FIGURE 10 Composites of wave filtered horizontal vorticity and wind fields band-pass in (a–c)the quick mode and (d–f) the slow mode, at 700 hPa. The time reference for compositing (H0) is taken when the tracked AEW crosses the 20°W. The horizontal structure is shown (a,d) 48 h prior to AEWs crossing 20°W, (b,e) 24 h prior to AEWs crossing 20°W, and (c,f) at the time AEWs cross 20°N. The contour lines show the unfiltered −10 and −8 m · s^{-1} zonal speed to locate the AEJ.

the two modes: the slow-mode composite shows a strong wave pattern with a maximum centered around 24°N, whereas the quick-mode composite peaks at 15°N. As opposed to the 6–9 day AEWs, their cyclonic phase is more intense (in terms of wave-filtered relative vorticity) than their anticyclonic phase. Waves detected in the slow mode are slightly less intense than their southern counterparts and are restrained between 20°N and 30°N. They are mainly active just outside the jet. A secondary center of activity is located inside the jet to the southeast of the main vorticity center. This might be explained by genesis processes, as some AEW-N are documented to be excited by wave activity on the south track (Pytharoulis & Thorncroft, 1999). The quick-mode structure displays wider vorticity centers with a better meridional alignment and a center of activity inside the AEJ, to the south of its most intense region. Both wave tracks display an intensification as the waves leave the coast.

Figure 11 shows the vertical structure of unfiltered vorticity for the slow mode and the quick mode, respectively. The composites are computed at the latitude of the centroid of each individual wave and are not computed at constant latitude. Above the continent, waves tracked in the slow mode peak at 850 hPa, consistently with the literature on north-track waves (Pytharoulis and Thorncroft, 1999). As they exit the coast, they transition to a higher altitude, and eventually peak at 700 hPa above the ocean. Waves tracked in the quick mode are more vertically coherent

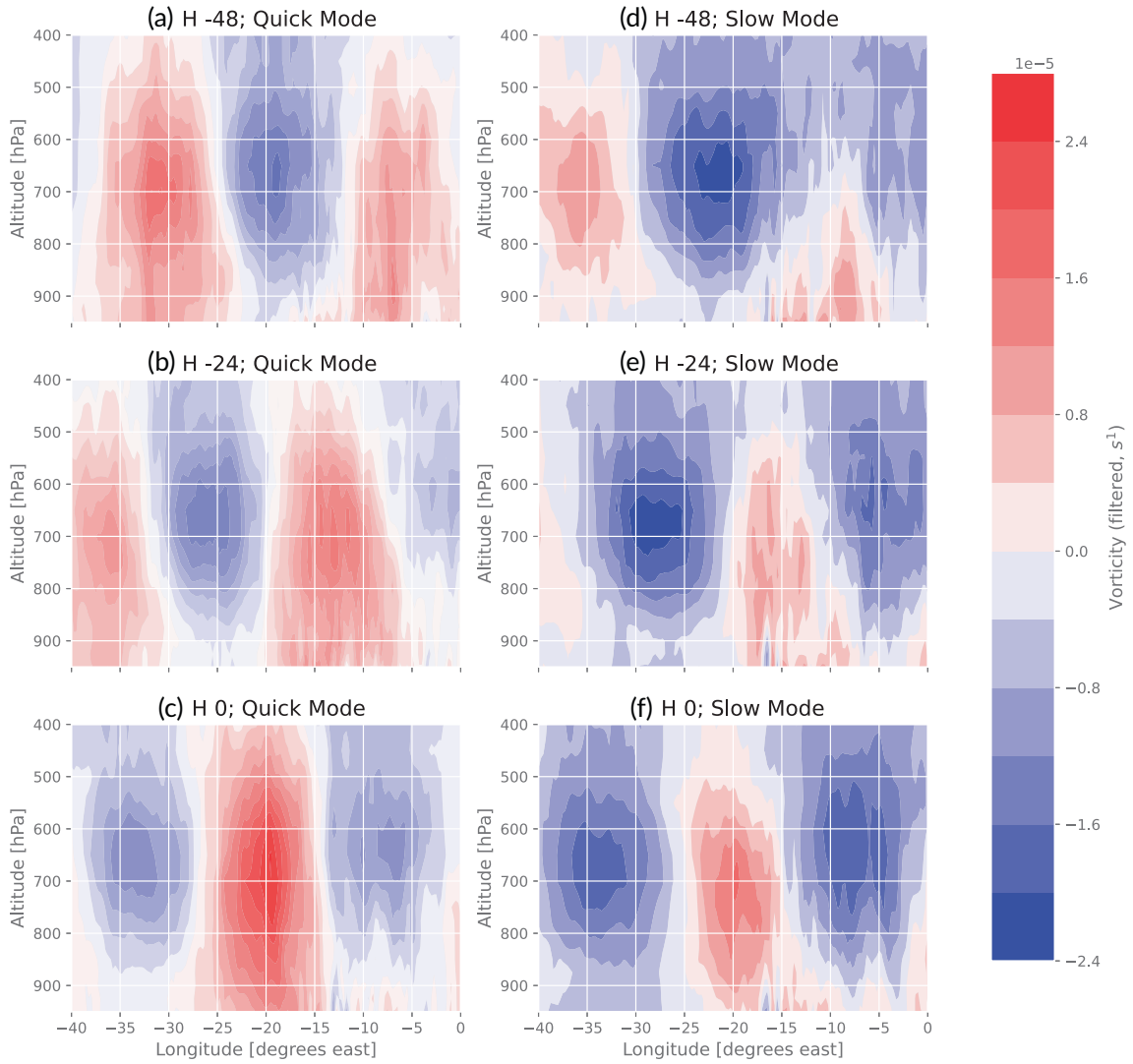

FIGURE 11 Longitude–height cross-section of vorticity composites for (a–c) quick-mode trajectories and (d–f) slow-mode trajectories. The time reference for compositing (H0) is taken when the tracked AEW crosses 20°W, at the latitude at which the trajectory crosses 20°W. The vertical structure is shown (a,d) 48 h prior to AEWs crossing 20°W, (b,e) 24 h prior to AEWs crossing 20°W, and (c,f) at the time AEWs cross 20°N.

48 hours before they exit the coast, displaying a strongly barotropic structure. They also intensify in the whole column as they leave the coast and remain at approximately constant altitudes.

4 | CYCLOGENESIS

Jonville *et al.* (2024) documented how the interaction between AEW-S and AEW-N could play a role in inhibiting cyclogenesis in the case of *Pierre-Henri*, or favoring it in the case of *Peter*. The fact that this type of interaction between the two wave tracks plays a role in tropical cyclogenesis has already been documented in the literature, especially when an AEW-N and an AEW-S merge to form a single anomaly of positive vorticity. Ross et al. (2007) mentioned that the mergers could intensify the circulation associated with the waves and favor genesis (Ross and Krishnamurti, 2007). Wu *et al.* (2013) mentioned that the interaction between the two tracks could result in more coherence between the low-level circulation and the jet-level circulation. Duvel (2021) also discussed how the vertical development of AEWs is necessary for TC genesis to be catalysed by the merger of north-track and south-track vortices. This process can help the vertical development and alignment of the wave pouch (Hankes *et al.*, 2015). As we have seen in the previous section, the quick-mode ∪ slow-mode tracking discussed in this article allows for the detection of more waves. This is especially true when one wave track dominates the signal.

Does this new method offer an opportunity to identify more AEW-N/AEW-S interactions in the context of tropical cyclogenesis? In order to get insights into the role of mergers in TC genesis when accounting for the results of the automated algorithm presented here over 30+ years, we compare the results obtained with the four different methods discussed in this article for tracking AEWs: 2–10 day tracking, quick-mode tracking, slow-mode tracking, and quick-mode ∪ slow-mode tracking (aggregating the results of quick- and slow-mode tracking).

Figure 12 shows the proportion of TCs that match an AEW-N, an AEW-S, or a merger. Most of the AEWs that are linked to TC genesis can be detected using either 2–10 day tracking or quick-mode tracking. Using 2–10 day tracking, 60.8% of TCs match an AEW from any wave track and for quick-mode tracking the proportion is 58.5% (Figure 12d). It is of the same order of magnitude as in the literature. Russell *et al.* (2017) found that 75% of TCs were related to an AEW, while Chen et al. (2008) found 62% and Enyew et al. (2022) 50.3%. On the other hand, only 30.7% of TCs match an AEW when using slow-mode tracking. Using quick-mode tracking ∪ slow-mode tracking, the proportion of TCs explained by an AEW reaches 63.7%. The use of quick-mode tracking ∪ slow-mode tracking only increases the number of TCs explained by AEWs by three base points compared with 2–10 day tracking. The trends are similar for AEW-S (Figure 12c). They are detected with 2–10 day tracking and quick-mode tracking as well. The fact that

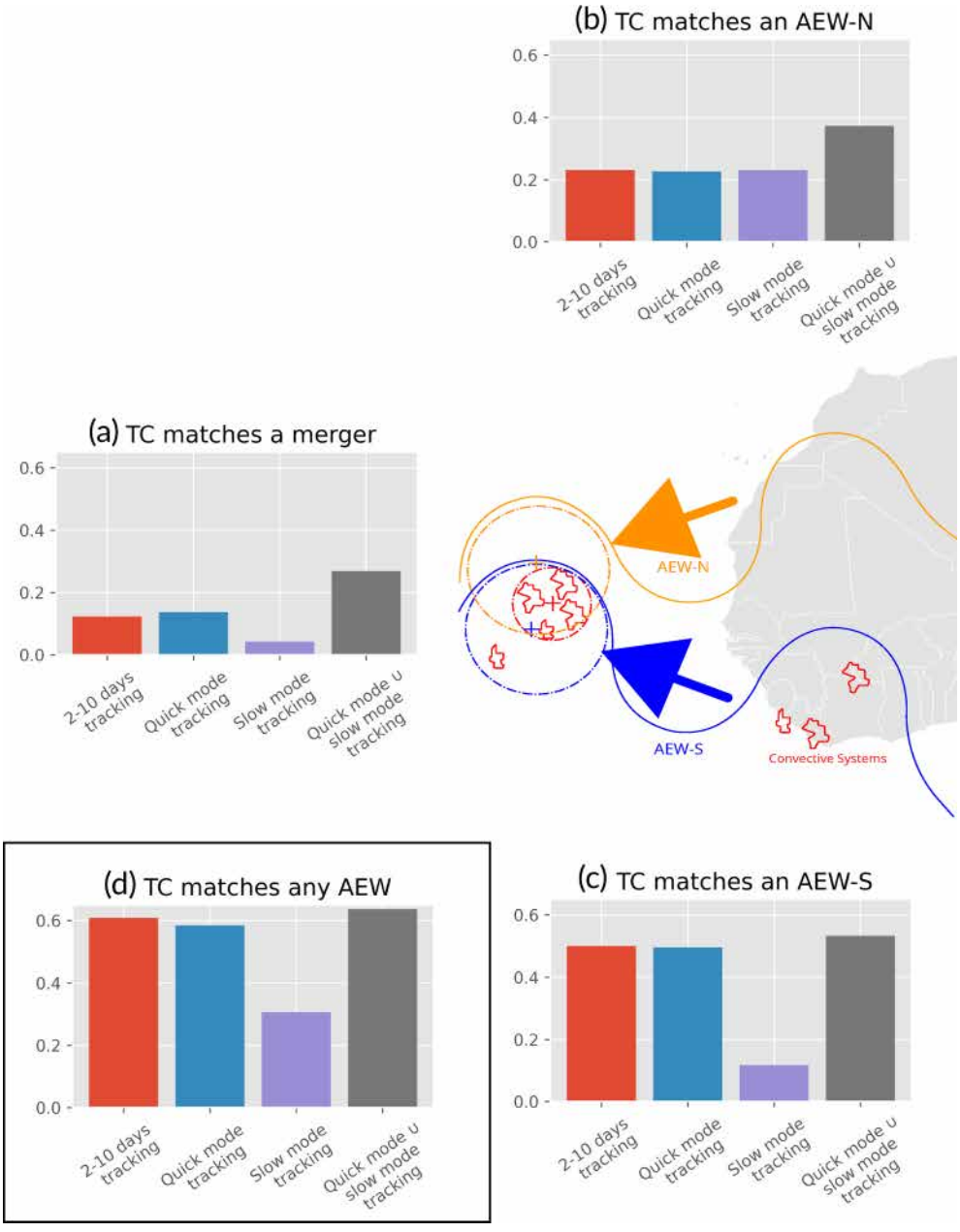

FIGURE 12 Proportion of TCs that match AEWs for the different tracking methods. A TC is said to match a merger if it matches both an AEW-N and an AEW-S (background drawing). (a) Proportion of TCs that match a merger. (b) Proportion of TCs that match an AEW-N. (c) Proportion of TCs that match an AEW-S. (d) Proportion of TCs that match any AEW (in a black box, as this case is not represented in the conceptual background drawing).

only a few TCs match an AEW-S using slow-mode tracking shows that the slow-mode period range is not suited for south-track dynamics. Regarding north-track dynamics (Figure 12b), 2–10 day tracking, quick-mode tracking, and slow-mode tracking detect about as many AEW-N in relation to TC genesis, but, in that specific case, quick- and slow-mode tracking prove to be quite complementary: joining their trajectories with quick-mode tracking ∪ slow-mode tracking results in an increased detection of AEW-N in relation to tropical cyclogenesis by 60% compared with the other methods. Those extra AEW-N are observed mainly at times when an AEW-S is also active, as most of them are mergers.

The number of TCs that match a merger (Figure 12a) detected using quick-mode ∪ slow-mode tracking is greater by 120% than that obtained with the commonly used 2–10 day band-pass filter, increasing from 12.3% to 26.9%. Hankes *et al.* (2015) found that 25% of TCs that formed east of 40°W between 1989 and 2010 were linked to a merger. If we carry out our analysis with this criterion on longitude, using 2–10 day tracking we find that 19.6% of TCs match a merger, less than half as many as obtained with quick-mode ∪ slow-mode tracking, that is, 45.1%. In this 31-year dataset, quick-mode ∪ slow-mode tracking has thus improved the detection of matches between TCs and AEW mergers. This conclusion is robust and holds when modifying the distance threshold between two interacting objects (see Appendix for a sensitivity analysis).

The efficiency of genesis of a type of AEW can now be defined as the ratio of the number of this type of AEW that match a TC over the total number of this type of AEW. These statistics are shown in Figure 13a,b. They are sensitive to the distance threshold chosen for the detection of mergers, but are qualitatively robust (see Appendix for

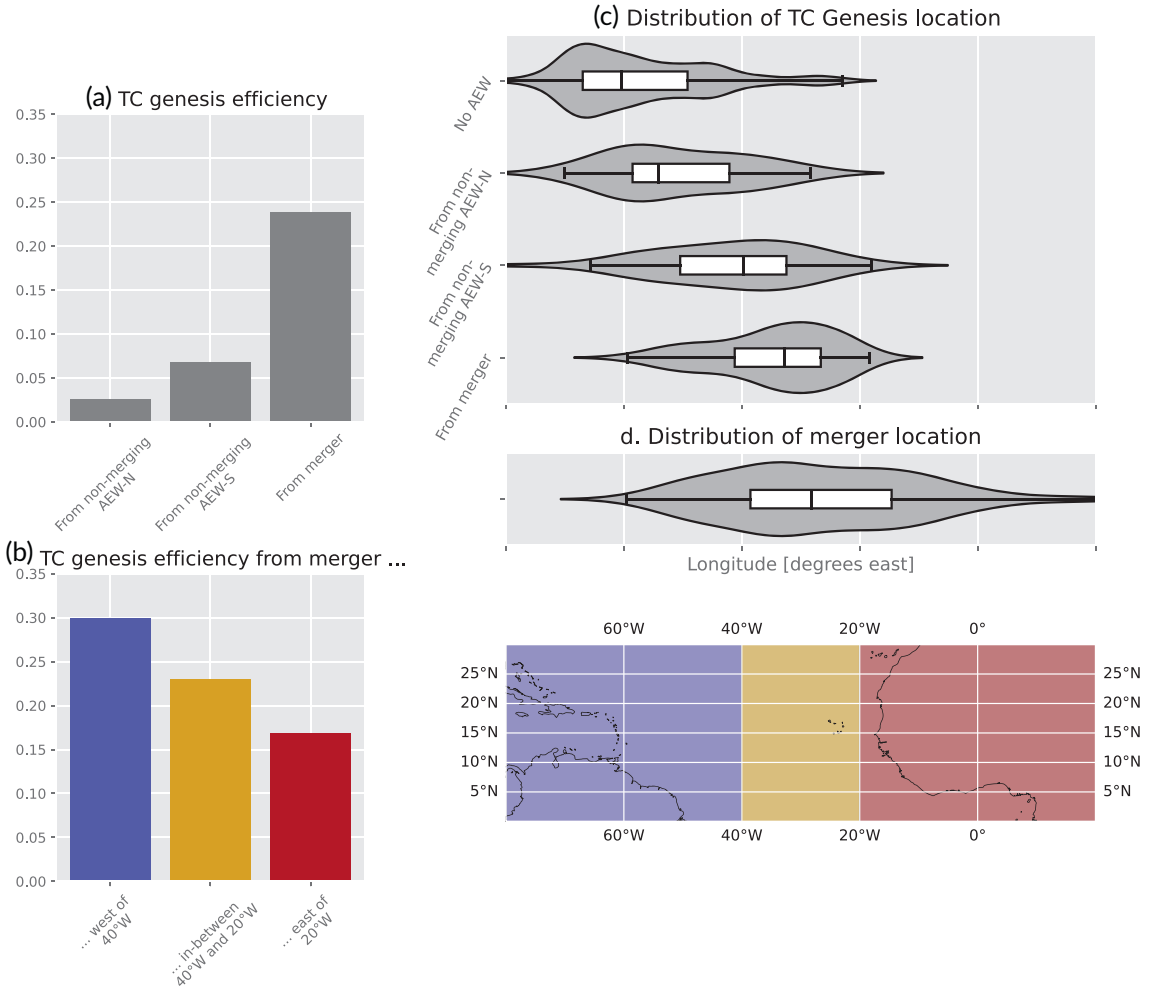

FIGURE 13 TC genesis efficiency and location depending on type of precursor, using quick-mode ∪ slow-mode tracking. (a) Genesis efficiency depending on type of AEW. (b) Genesis efficiency from mergers depending on the location of the merger. (c) Distribution of TC genesis location depending on the type of precursor. (d) Distribution of merger location. Genesis efficiency is defined as the number of genesis cases from a given precursor over the total number of the detected precursor (example: right bar of panel (a) is computed as the number of TCs developing from a merger over the total number of mergers).

more details). 8.9% of all AEW-N and 3.4% of non-merging AEW-N match a TC. On the south track, 13.4% of all AEW-S and 8.8% of non-merging AEW-S match a TC. Mergers are precursors that are 6.8 times more efficient for TC genesis than non-merging AEW-N and 2.7 times more efficient than non-merging AEW-S, with 23.4% of them matching a TC. The later the merger occurs, the more efficient it is at evolving in a TC (see Figure 13b): when the merger occurs east of 20°W, it has a 16.9% chances of triggering cyclogenesis (65 mergers detected). The proportion increases to 23.0% between 20°W and 40°W (84 mergers detected), and reaches 30.0% west of 40°W (52 mergers detected). According to the conceptual framework developed by Duvel (2021), the AEW-N bring the low-level vorticity and the AEW-S the mid-level vorticity, so that the whole column is preconditioned for TC genesis. Our results highlight that this transition from a merger to a TC is not automatic. In Jonville *et al.* (2024), we have shown that, for *Pierre-Henri*, an AEW that did not develop into a TC, the merger favored the incorporation of dry air inside the AEW-S, inhibiting genesis. Taking thermodynamic effects into consideration might help us understand the relation between the longitude of occurrence of the merger and TC genesis efficiency: as the AEW-N moves westward, it may be humidified by surface fluxes from the ocean, thereby decreasing the inhibiting effect of the AEW-N.

However, most mergers occur on the eastern side of the basin (see Figure 13d.). The quantity of mergers more than compensate for the loss of efficiency: the mean location of mergers is at 26.5°W, with 75% of mergers occurring east of 38°W. Therefore, the mean location of TC genesis from mergers is at 33.8°W (standard deviation 9.8°), eastward of the TC genesis location from AEW-S only (41.5°W, standard deviation 13.5°) and from AEW-N only (50.4°N, standard deviation 11.8°; see Figure 13c). Duvel (2021) found similar results, with most cyclogenesis from mergers occurring east of 30°W. The difference between the locations of AEW-N and AEW-S genesis was already discussed by Chen *et al.* (2008). They found that AEW-N tend to travel further across the basin before triggering TC genesis, as they are dryer and evolve above colder waters than AEW-S when they exit the African coast.

5 | SUMMARY AND CONCLUSION

An automated tracking algorithm has been applied to a 31-year archive of ERA5 data (1991–2021). The results in terms of number of waves were comparable with the literature using the common 2–10 day band-pass filtering and in a region extending from 5°N–20°N. Extending the region of study to 30°N, we highlighted the existence of two distinct wave tracks with a minimum of trajectory density located around 18.2°N.

Most of the waves detected at 850 hPa using a 2–10 day filter propagate at 18°N, that is, between the two wave tracks identified at 700 hPa. 34% of 850-hPa wave centers are found to be vertically coherent with an AEW-S at 700 hPa, 31% with an AEW-N at 700 hPa. 35% are not attributed to any 700-hPa wave. The latter are associated with weaker relative vorticity in the whole column, therefore they are expected to impact cyclogenesis less than those AEW detected at 850 hPa that match a wave detected at 700 hPa. However, they show a weak signature at 700 hPa in the region of the north track. This motivated the development of the refined tracking method at 700 hPa, as the commonly used 2–10 day tracking methods at 700 hPa miss AEW-N waves and do not allow us to distinguish between AEW-N and AEW-S at 850 hPa.

The composites of the wavelet power spectrum for 700-hPa AEWs on each track show significant differences in peak period for each track. This difference remains marked throughout the summer months. A seasonality in each peak intensity is observed and is found to be in good agreement with the seasonality of wave activity on each wave track (Duvel, 2021). From those results, two different period windows are defined from the 31-year ERA5 archive to isolate the signal from the south/quick wave mode (2.95–4.55 days) and the north/slow wave mode (4.55–6.35 days). A new tracking procedure is performed using an ad hoc band-pass filter for each period range. The tracking of the slow/north mode (respectively the quick/south mode) allows the identification of most of the tracks obtained north (respectively south) of 18.2°N when using the commonly used 2–10 day band-pass filter. The sum of the trajectory densities of the two modes shows the same features as the one obtained with the 2–10 day band-pass filter. This shows that distinguishing the two modes is a good way of separating the dynamics north of the AEJ from the dynamics south of the AEJ. Dynamic fields such as vorticity and wind speed are composited over the trajectories around the date when the vortices exit the West African continent. Differences in the dynamical characteristics for the two wave tracks are significant and consistent with the literature. AEWs tracked in the slow mode are weaker than those tracked in the quick mode, peak at a latitude around 24°N, and present a southward tilt in their trajectory. They peak at around 850 hPa above the continent, and present a strong upward trajectory as they undergo their continent-to-ocean transition. On the other hand, AEWs tracked in the quick mode peak around 15°N and show greater relative vorticity than their northern counterparts. They peak between 600 and 700 hPa and intensify as they exit the continent. Distinguishing quick

and slow modes allows us to separate the activities of the two wave tracks effectively and to highlight their specific characteristics.

We have then applied this method to the September 2021 case. As with the manual tracking performed by Jonville *et al.* (2024), the separation of quick and slow modes enabled the identification of north-track activity that was hindered by the dominant south-track signal when filtering using the 2–10 day band-pass filter. This offers the opportunity to study AEW-S/AEW-N mergers for a deeper archive (i.e., 30+ years). By applying a simple conceptual framework (assuming that two objects closer than a specified distance threshold interact) and using NHC best track data, we assess how tropical cyclogenesis is linked to AEW activity using several methods (2–10 day tracking, quick-mode tracking, slow-mode tracking, quick-mode ∪ slow-mode tracking). Results of 2–10 day tracking were comparable with the results of the literature on the link between AEWs and TCs in the Atlantic. Quick-mode tracking performed almost as well as 2–10 day tracking, whereas slow-mode tracking missed a lot of AEW–TC matches, suggesting that TCs are mainly linked to south wave activity, in accordance with the literature. Using quick-mode ∪ slow-mode tracking, we identified as many AEW-S/TC interactions overall, but the method increases by 80% the number of TCs that match an AEW-N and by 150% the number of TCs that match a merger. These trends are robust to the choice of distance threshold and are consistent with the observation made in the case study that quick-mode ∪ slow-mode tracking allows the detection of AEW-N in dominant south-track settings.

TCs that developed on the eastern side of the basin were especially prone to be related to a merger (45.1% of TC genesis related to a merger east of 40°W, mean longitude of genesis from merger 33.8°W). The mergers favor TC genesis with a significantly higher efficiency than AEW-S and AEW-N alone, as 23.4% of mergers triggered a TC, compared with only 3.4% of non-merging AEW-N and 8.8% of non-merging AEW-S. The further westward the mergers occur, the higher the efficiency, with 30% of mergers west of 40°W triggering a genesis. This may be explained by the fact that AEW-N contain dry air from the Sahara and tend to be moistened as they travel westward: if mergers occur too early, they can dry the circulation and inhibit cyclone formation, as discussed by Jonville *et al.* (2024) for *Pierre-Henri* in September 2021.

This study shows that the impact of AEW-N/AEW-S mergers might have been underestimated. It proposes a new method to detect such interactions systematically by separating the channels of detection of each AEW track. This method is more robust than the detection of AEW-N at 850 hPa, as the latter detects as many low-level activity centers associated with AEW-S as with AEW-N (see Figure 7). It also allows following of AEW-N for longer over the ocean, where they have a greater impact on tropical cyclogenesis. Some AEW-N are still missed at 700 hPa, but they show a weaker relative vorticity in the whole column and are therefore expected to have less of an impact on tropical cyclogenesis than the waves that are detected at both levels. It is important to note that this detection method is likely overcounting AEWs, therefore caution applies when using the method to examine AEW frequency. The modality of interactions between AEW-N and AEW-S and the underlying physical processes still have to be investigated with a climatological outlook, extending the analysis conducted in Jonville *et al.* (2024) in the case studies. Especially, a more systematic analysis of the balance between inhibiting processes (advection of dry air by the AEW-N) and catalysing processes (dynamical invigoration of low-level dynamics, warming of the core, creation of a wave pouch in the whole column, etc.) has to be conducted.

ACKNOWLEDGEMENTS

The airborne component of CADDIWA was supported by the French national program LEFE/INSU of the Centre National de la Recherche Scientifique (CNRS), Centre National d'Etudes Spatiales (CNES), the European Space Agency (ESA) and the Institut Pierre-Simon Laplace (IPSL). The CNES/TOSCA projects funding these activities are called CADDIWA and IASI—Aerosols. T. Jonville acknowledges the French Ministry for the Environmental Transition (MTECT) for funding his PhD. E. Cornillault and P. Peyrillé acknowledge Météo France for their funding. The authors thank the anonymous reviewers for their comments and suggestions, which have greatly improved the article.

FUNDING INFORMATION

Centre National d'Etudes Spatiales (CNES); European Space Agency (ESA, RFP/3-16595/20/NL/FF/ab); National program LEFE of the Institut des Sciences de l'Univers (INSU) of Centre National de la Recherche Scientifique (CNRS); Institut Pierre-Simon Laplace (IPSL); Météo France; Ministère de la Transition Ecologique et de la Cohésion des Territoires (MTECT).

DATA AVAILABILITY STATEMENT

Data available on request from the authors.

ORCID

Tanguy Jonville https://orcid.org/0009-0004-8430-0285
Erwan Cornillault https://orcid.org/0000-0003-2949-2486

REFERENCES

Agudelo, P.A., Hoyos, C.D., Curry, J.A. & Webster, P.J. (2011) Probabilistic discrimination between large-scale environments of intensifying and decaying African easterly waves. *Climate Dynamics*, 36, 1379–1401.

Arnault, J. & Roux, F. (2010) Comparison between two case studies of developing and nondeveloping African easterly waves during NAMMA and AMMA/SOP-3: absolute vertical vorticity budget. *Monthly Weather Review*, 138, 1420–1445.

Arnault, J. & Roux, F. (2011) Characteristics of African easterly waves associated with tropical cyclogenesis in the Cape Verde Islands region in July-august-September of 2004-2008. *Atmospheric Research*, 100, 61–82.

Asaadi, A., Brunet, G. & Yau, M.K. (2016) On the dynamics of the formation of the kelvin Cat's-eye in tropical cyclogenesis. Part I: climatological investigation. *Journal of the Atmospheric Sciences*, 73, 2317–2338.

Asaadi, A., Brunet, G. & Yau, M.K. (2017) On the dynamics of the formation of the kelvin Cat's-eye in tropical cyclogenesis. Part II: numerical simulation. *Journal of the Atmospheric Sciences*, 73, 2339–2359.

Bain, C.L., Williams, K.D., Milton, S.F. & Heming, J.T. (2014) Objective tracking of African easterly waves in met Office models. *Quarterly Journal of the Royal Meteorological Society*, 140, 47–57.

Bercos-Hickey, E., Nathan, T.R. & Chen, S.-H. (2017) Saharan dust and the African easterly jet–African easterly wave system: structure, location and energetics. *Quarterly Journal of the Royal Meteorological Society*, 143, 2797–2808.

Berry, G., Thorncroft, C. & Hewson, T. (2007) African easterly waves during 2004—analysis using objective techniques. *Monthly Weather Review*, 135, 1251–1267.

Bié, A.J. & de Camargo, R. (2023) Tropical cyclones position and intensity in the Southwest Indian Ocean as represented by CFS and ERA5 atmospheric reanalysis datasets. *International Journal of Climatology*, 43, 4532–4551.

Brammer, A. & Thorncroft, C.D. (2015) Variability and evolution of African easterly wave structures and their relationship with tropical cyclogenesis over the eastern Atlantic. *Monthly Weather Review*, 143, 4975–4995.

Brammer, A., Thorncroft, C.D. & Dunion, J.P. (2018) Observations and predictability of a nondeveloping tropical disturbance over the eastern Atlantic. *Monthly Weather Review*, 146, 3079–3096.

Brient, F., Couvreux, F., Villefranque, N., Rio, C. & Honnert, R. (2019) Object-oriented identification of coherent structures in large Eddy simulations: importance of downdrafts in stratocumulus. *Geophysical Research Letters*, 46, 2854–2864.

Burpee, R.W. (1972) The origin and structure of easterly waves in the lower troposphere of North Africa. *Journal of the Atmospheric Sciences*, 29, 77–90.

Chen, S.-H. & Liu, Y.-C. (2014) The relation between dry vortex merger and tropical cyclone genesis over the Atlantic Ocean. *Journal of Geophysical Research: Atmospheres*, 119, 11,641–11,661.

Chen, T.-C. (2006) Characteristics of African easterly waves depicted by ECMWF reanalyses for 1991–2000. *Monthly Weather Review*, 134, 3539–3566.

Chen, T.-C., Wang, S.-Y. & Clark, A.J. (2008) North Atlantic hurricanes contributed by African easterly waves north and south of the African easterly jet. *Journal of Climate*, 21, 6767–6776.

Cornforth, R.J., Hoskins, B.J. & Thorncroft, C.D. (2009) The impact of moist processes on the African easterly jet–African easterly wave system. *Quarterly Journal of the Royal Meteorological Society*, 135, 894–913.

Danso, D.K., Patricola, C.M. & Bercos-Hickey, E. (2022) Influence of African easterly wave suppression on Atlantic tropical cyclone activity in a convection-permitting model. *Geophysical Research Letters*, 49, e2022GL100590.

De Felice, P., Viltard, A., Monkam, D. and Ouss, C. (1990) *Characteristics of North African 6-9 Day Waves During Summer 1981*, 118, 2624–2633.

Diedhiou, A. (1998) *Étude Des Régimes d'ondes d'est et de Leurs Interactions Avec La Convection En Afrique de l'Ouest et Sur l'Atlantique Tropical*. Paris: These de doctorat, p. 12.

Diedhiou, A., Janicot, S., Viltard, A. & de Félice, P. (2002) Energetics of easterly wave disturbances over West Africa and the tropical Atlantic: a climatology from the 1979–95 NCEP/NCAR reanalyses. *Climate Dynamics*, 18, 487–500.

Diedhiou, A., Janicot, S., Viltard, A., de Felice, P. & Laurent, H. (1999) Easterly wave regimes and associated convection over West Africa and tropical Atlantic: results from the NCEP/NCAR and ECMWF reanalyses. *Climate Dynamics*, 15, 795–822.

Diedhiou, A., Machado, L.A.T. & Laurent, H. (2010) Mean kinematic characteristics of synoptic easterly disturbances over the Atlantic. *Advances in Atmospheric Sciences*, 27, 483–499.

Dieng, A.L., Sall, S.M., Eymard, L., Leduc-Leballeur, M. & Lazar, A. (2017) Trains of African Easterly Waves and Their Relationship to tropical cyclone genesis in the eastern Atlantic. *Monthly Weather Review*, 145, 599–616.

Dunkerton, T.J., Montgomery, M.T. & Wang, Z. (2009) Tropical cyclogenesis in a tropical wave critical layer: easterly waves. *Atmospheric Chemistry and Physics*, 9, 5587–5646.

Duvel, J.-P. (2021) On vortices initiated over West Africa and their impact on North Atlantic tropical cyclones. *Monthly Weather Review*, 149, 585–601.

Fink, A.H. & Reiner, A. (2003) Spatiotemporal variability of the relation between African easterly waves and west African squall lines in 1998 and 1999. *Journal of Geophysical Research: Atmospheres*, 108, (D11), 4332.

Flamant, C., Chaboureau, J.-P., Delanoë, J., Gaetani, M., Jamet, C., Lavaysse, C. et al. (2024) Cyclogenesis in the tropical Atlantic: first scientific highlights from the clouds-atmospheric dynamics-dust interactions in West Africa (CADDIWA) field campaign (accepted). *Bulletin of the American Meteorological Society*, 105, E387–E417.

Frank, N.L. (1970) Atlantic tropical systems of 1969. *Monthly Weather Review*, 98, 307–314.

Grogan, D.F.P., Nathan, T.R. & Chen, S.-H. (2016) Effects of Saharan dust on the linear dynamics of African easterly waves. *Journal of the Atmospheric Sciences*, 73, 891–911.

Hankes, I., Wang, Z., Zhang, G. & Fritz, C. (2015) Merger of African easterly waves and formation of Cape Verde storms. *Quarterly Journal of the Royal Meteorological Society*, 141, 1306–1319.

Hersbach, H., Bell, B., Berrisford, P., Hirahara, S., Horányi, A., Muñoz-Sabater, J. et al. (2020) The ERA5 global reanalysis. *Quarterly Journal of the Royal Meteorological Society*, 146, 1999–2049.

Hopsch, S.B., Thorncroft, C.D. & Tyle, K.R. (2010) Analysis of African easterly wave structures and their role in influencing tropical cyclogenesis. *Monthly Weather Review*, 138, 1399–1419.

Janiga, M.A. & Thorncroft, C.D. (2013) Regional differences in the kinematic and thermodynamic structure of African easterly waves. *Quarterly Journal of the Royal Meteorological Society*, 139, 1598–1614.

Jenkins, M.A. (1995) The cold-Core temperature structure in a tropical easterly wave. *Journal of the Atmospheric Sciences*, 52, 1168–1177.

Jonville, T., Flamant, C. & Lavaysse, C. (2024) Dynamical study of three African easterly waves in September 2021. *Quarterly Journal of the Royal Meteorological Society*, 2489–2509.

Kiladis, G.N., Thorncroft, C.D. & Hall, N.M.J. (2006) Three-dimensional structure and dynamics of African easterly waves. Part I: observations. *Journal of the Atmospheric Sciences*, 63, 2212–2230.

Kiladis, G.N., Wheeler, M.C., Haertel, P.T., Straub, K.H. & Roundy, P.E. (2009) Convectively coupled equatorial waves. *Reviews of Geophysics*, 47, RG2003.

Knapp, K.R., Kruk, M.C., Levinson, D.H., Diamond, H.J. & Neumann, C.J. (2010) The international best track archive for climate stewardship (IBTrACS): unifying tropical cyclone data. *Bulletin of the American Meteorological Society*, 91, 363–376.

Kwon, H.J. & Mak, M. (1990) A study of the structural transformation of the African easterly waves. *Journal of the Atmospheric Sciences*, 47, 277–292.

Landsea, C.W. (1993) A climatology of intense (or major) Atlantic hurricanes. *Monthly Weather Review*, 121, 1703–1713.

Landsea, C.W. & Franklin, J.L. (2013) Atlantic hurricane database uncertainty and presentation of a new database format. *Monthly Weather Review*, 141, 3576–3592.

Lavaysse, C., Flamant, C., Janicot, S. & Knippertz, P. (2010) Links between African easterly waves, midlatitude circulation and intraseasonal pulsations of the west African heat low. *Quarterly Journal of the Royal Meteorological Society*, 136, 141–158.

Lee, G.R., Gommers, R., Waselewski, F., Wohlfahrt, K. & O'Leary, A. (2019) PyWavelets: a python package for wavelet analysis. *Journal of Open Source Software*, 4, 1237.

Liu, Y., Liang, X.S. & Weisberg, R.H. (2007) Rectification of the bias in the wavelet power Spectrum. *Journal of Atmospheric and Oceanic Technology*, 24, 2093–2102.

Matsuno, T. (1966) Quasi-geostrophic motions in the equatorial area. *Journal of the meteorological Society of Japan. Ser. II*, 44, 25–43.

Mekonnen, A., Thorncroft, C.D. & Aiyyer, A.R. (2006) Analysis of convection and its association with African easterly waves. *Journal of Climate*, 19, 5405–5421.

Ocasio, K.M.N., Brammer, A., Evans, J.L., Young, G.S. & Moon, Z.L. (2021) Favorable monsoon environment over eastern Africa for subsequent tropical cyclogenesis of African easterly waves. *Journal of the Atmospheric Sciences*, 78, 2911–2925.

Pytharoulis, I. & Thorncroft, C. (1999) The low-level structure of African easterly waves in 1995. *Monthly Weather Review*, 127, 2266–2280.

Reed, R.J., Hollingsworth, A., Heckley, W.A. & Delsol, F. (1988) An evaluation of the performance of the ECMWF operational system in Analyzing and forecasting easterly wave disturbances over Africa and the tropical Atlantic. *Monthly Weather Review*, 116, 824–865.

Ross, R. & Krishnamurti, T. (2007) Low-level African easterly wave activity and its relation to Atlantic tropical cyclogenesis in 2001. *Monthly Weather Review*, 135, 3950–3964.

Roundy, P.E. & Frank, W.M. (2004) A climatology of waves in the equatorial region. *Journal of the Atmospheric Sciences*, 61, 2105–2132.

Russell, J.O., Aiyyer, A., White, J.D. & Hannah, W. (2017) Revisiting the connection between African easterly waves and Atlantic tropical cyclogenesis. *Geophysical Research Letters*, 44, 587–595.

Rutherford, B., Boothe, M.A., Dunkerton, T.J. & Montgomery, M.T. (2018) Dynamical properties of developing tropical cyclones using Lagrangian flow topology. *Quarterly Journal of the Royal Meteorological Society*, 144, 218–230.

Satoh, M., Nihonmatsu, R. & Kubokawa, H. (2013) Environmental conditions for tropical cyclogenesis associated with African easterly waves. *Scientific Online Letters on the Atmosphere*, 9, 120–124.

Schreck, C.J., Molinari, J. & Aiyyer, A. (2012) A global view of equatorial waves and tropical cyclogenesis. *Monthly Weather Review*, 140, 774–788.

Thomson, R.E. & Emery, W.J. (2014) Chapter 6 - Digital Filters. In: Thomson, R.E. & Emery, W.J. (Eds.) *Data analysis methods in physical oceanography*, Third edition. Boston: Elsevier, pp. 593–637.

Thorncroft, C. & Hodges, K. (2001) African easterly wave variability and its relationship to Atlantic tropical cyclone activity. *Journal of Climate*, 14, 1166–1179.

Thorncroft, C.D. (1995) An idealized study of African easterly waves. III: more realistic basic states. *Quarterly Journal of the Royal Meteorological Society*, 121, 1589–1614.

Thorncroft, C.D., Hall, N.M.J. & Kiladis, G.N. (2008) Three-dimensional structure and dynamics of African easterly waves. Part III: genesis. *Journal of the Atmospheric Sciences*, 65, 3596–3607.

Thorncroft, C.D. & Hoskins, B.J. (1994) An idealized study of African easterly waves. I: a linear view. *Quarterly Journal of the Royal Meteorological Society*, 120, 953–982.

Torrence, C. & Compo, G.P. (1998) A practical guide to wavelet analysis. *Bulletin of the American Meteorological Society*, 79, 61–78.

Wang, Z., Dunkerton, T.J. & Montgomery, M.T. (2012) Application of the marsupial paradigm to tropical cyclone formation from Northwestward-propagating disturbances. *Monthly Weather Review*, 140, 66–76.

Wang, Z., Montgomery, M.T. & Dunkerton, T.J. (2010) Genesis of pre–hurricane Felix (2007). Part I: the role of the easterly wave critical layer. *Journal of the Atmospheric Sciences*, 67, 1711–1729.

Wu, M.-L.C., Reale, O. & Schubert, S.D. (2013) A characterization of African easterly waves on 2.5–6-day and 6–9-day time scales. *Journal of Climate*, 26, 6750–6774.

How to cite this article: Jonville, T., Cornillault, E., Lavaysse, C., Peyrillé, P. & Flamant, C. (2024) Distinguishing north and south African Easterly Waves with a spectral method: Implication for tropical cyclogenesis from mergers in the North Atlantic. *Quarterly Journal of the Royal Meteorological Society*, 1–25. Available from: https://doi.org/10.1002/qj.4909

APPENDIX A. CHOICE OF THRESHOLD FOR 2–10 DAY TRACKING

Table A1 shows the number of waves detected by the algorithm depending on the thresholds, in terms of both vorticity and lifespan. It is important to note that, when two features touch each other, they are merged by the algorithm, which is often noticed for an intensity threshold that is too low (not shown). In contrast, a threshold that is too high can eliminate too many objects. Results are put in context with the literature by restricting the region of study to be comparable with that in the literature (i.e., 20°N instead of 30°N). Threshold pairs $1.75 \times 10^{-5} \cdot s^{-1}$/4 days and $2.00 \times 10^{-5} \cdot s^{-1}$/3 days give results comparable with the literature. However, in specific cases (see supplementary materials for more details), the $1.75 \times 10^{-5} \cdot s^{-1}$/4 days tend to merge features that should remain distinct. The thresholds $2.00 \times 10^{-5} \cdot s^{-1}$/3 days are kept in the following for the 2–10 day period window. Since this article focuses on the characteristics of AEW-N and AEW-S, the region of study is extended in the rest of this article to 30°N to capture all AEW-N activity.

Two sets of thresholds are good candidates to maintain consistency between the tracking used and the literature:

- **set A:** $1.75 \times 10^{-5} \cdot s^{-1}$, 4 days with 27.8 AEWs detected per JJAS;
- **set B:** $2.00 \times 10^{-5} \cdot s^{-1}$, 3 days with 30.0 AEWs detected per JJAS.

To arbitrate between the two sets of thresholds and to keep this study in the context of the one conducted in Jonville *et al.* (2024), we compared the performance of the two sets of thresholds in September 2021. The troughs associated with *Peter* and *Pierre-Henri* come closer on the Hovmöller diagram after they have passed 30°W. This configuration leads to the merger of the two troughs when applying a mask with set A. This then prevents good following of the object: as the location of an object is taken as the centroid of all points passing the threshold, before 30°W the centroid for set A is at the mid-distance of *Pierre-Henri* and *Peter*, at the longitude of the ridge that separates the two objects. On the other hand, for set B the two objects are not merged, and the two trough trajectories are consistent with the Hovmöller diagram. Thus, set B is retained for this study.

TABLE A1 Choice of lifespan and intensity thresholds. The number of waves detected is shown for different sets of thresholds when applying the tracking algorithm for the band-pass period 2–10 days. The algorithm is applied here to a domain bounded to 20°N for this comparative analysis, as in most of the methods described in the literature. Intensity threshold units for our algorithm are expressed in $10^{-5} \cdot s^{-1}$.

Intensity threshold (relative vorticity)	Lifespan threshold	Number of waves
Threshold 1.75	> 3 days	44.5 per JJAS
	> 4 days	27.8 per JJAS
Threshold 2.00	> 3 days	30.0 per JJAS
	> 4 days	18.3 per JJAS

TABLE B1 Choice of thresholds for quick- and slow-mode tracking.

Intensity threshold (relative vorticity)	Lifespan threshold	Number of waves
Threshold 1.00	> 3 days	63.0 per JJAS
	> 4 days	45.1 per JJAS
Threshold 1.25	> 3 days	40.8 per JJAS
	> 4 days	27.8 per JJAS
Threshold 1.50	> 3 days	24.0 per JJAS
	> 4 days	14.3 per JJAS

APPENDIX B. CHOICE OF THRESHOLD FOR SLOW AND QUICK MODES

As for the 2–10 day tracking, it is necessary to choose the threshold for the intensity and lifespan when filtering on the quick and slow modes. Since the period band is narrower, it contains less energy and it is expected that, to maintain a consistent number of waves, the intensity threshold has to be lowered compared with 2–10 day filtering. The idea here is to keep the number of south-track waves in the quick mode as close as possible to the number of south-track waves in the 2–10 day tracking. We keep the same set of thresholds for quick and slow modes for intercomparability reasons. Table B1 shows the number of AEW tracks south of 20°N for different sets of thresholds. The closest value to that of the 2–10 day tracking performed in this study is found for the $1.25 \times 10^{-5} \cdot s^{-1}$, 4 days threshold.

APPENDIX C. SENSITIVITY ANALYSIS ON FREQUENCY WINDOWS FOR QUICK- AND SLOW-MODE TRACKING

To ensure the robustness of the results with respect to the choice of the selected frequency window, the results of the tracking algorithm for different frequency windows for the northern and southern modes are compared in Table C1. Each window is determined by selecting the period values for which the 700-hPa meridian wind spectra and the 700-hPa relative vorticity spectra

TABLE C1 Sensitivity analysis for the frequency window of quick- and slow-mode tracking.

Period window	Corresponding threshold (relative vorticity, in s^{-1})	Number of AEW per JJAS	Proportion to reference	Proportion of common tracks	Latitude bias to reference	Mean phasing duration
Quick Mode (Tracking of reference V77 2.95–4.55 days, threshold $1.25 \times 10^{-5} \cdot s^{-1}$, 43.12 AEWs per JJAS)						
V85 (3.21–4.51 days)	1.15	39.9	92.4%	85.6%	−1.65°	5.18 days
V90 (3.34–4.39 days)	1.00	45.2	105%	79.8%	−1.73°	4.61 days
V95 (3.48–4.17 days)	0.85	41.5	96.2%	70.1%	−1.13°	4.25 days
VO85 (2.00–4.73 days)	1.50	47.2	109%	84.4%	−1.57°	4.04 days
VO90 (2.00–4.48 days)	1.50	42.8	99.3%	79.3%	−1.38°	4.17 days
VO95 (2.68–3.89 days)	1.10	46.22	107.2%	77.3%	−1.25°	3.84 days
Slow Mode (Tracking of reference V77 4.55–6.35 days, threshold $1.25 \times 10^{-5} \cdot s^{-1}$, 20.7 AEWs per JJAS)						
V85 (4.85–6.15 days)	1.05	21.7	105%	76.4%	−0.70°	4.88 days
V90 (4.98–6.00 days)	1.00	20.1	97.0%	69.8%	−0.87°	4.65 days
V95 (5.14–5.86 days)	0.80	20.4	98.6%	58.0%	0.17 °	4.11 days
VO85 (4.45–6.30 days)	1.30	20.1	97.3%	87.3%	−0.69°	5.42 days
VO90 (4.67–6.11 days)	1.15	21.5	104%	84.7%	−0.61°	5.33 days
VO95 (4.90–5.93 days)	0.95	21.0	101%	66.7%	−0.69°	4.59 days

respectively reach 85%, 90%, and 95% of their peak values for the northern waves on one hand and the southern waves on the other hand. These frequency windows are hereafter labeled V85, V90, V95 for the meridian wind and VO85, VO90, VO95 for the relative vorticity.

Next, the trajectories are compared while maintaining a nearly constant number of detected trajectories. To do this, we determine the vorticity threshold value for which the number of detected AEWs is closest to the reference. This adjustment compensates for the fact that the narrower the frequency window, the lower the energy available, and therefore the lower the amplitude of the filtered signal.

The proportion of common trajectories between the reference and another tracking is defined by counting the number of trajectories that are in phase between the two datasets (recall that two trajectories are in phase when they are located within 3° of longitude from each other at a given date). The denominator of this ratio is the maximum number of trajectories that can be in phase, that is, the smaller number of detected AEWs between the two trackings compared. Since this measure does not provide information on the difference in latitude between the centers or the duration of phasing, these details are also included in the table for reference.

Despite the variety of frequency windows tested, all trackings contain a majority of common trajectories with their reference tracking (over 70% and up to 87.3%, except for the slow-mode V95 and VO95 windows at 58.0% and 66.7%, respectively). The most conservative frequency windows (V95 and VO95) tend to be associated with the lowest intensity thresholds and the poorest performance. This might be explained by the fact that they are too selective and miss trajectories with slight variations of peak period and because they are too narrow to contain enough energy to have a good signal-to-noise ratio. When in phase, tracked centers also have close latitudes (the average latitude difference between common trajectories is less than 2°, with a bias towards the Equator for the quick mode and an average latitude difference of less than 1°, with a similar equatorward bias for slow-mode trajectories). Finally, the trajectories remain in phase with their reference for more than 4 days (except for the VO95 window in quick mode, with an average phasing duration of 3.84 days). All these factors indicate that the same objects are detected for the quick and slow modes regardless of the chosen frequency window. The trajectories used in the rest of the study are therefore robust with respect to the frequency windows.

APPENDIX D. LANCZOS, FOURIER, OR BUTTERWORTH FILTERS

When narrowing the band of frequency for the filter, the signal might be subject to Gibbs effects (Thomson & Emery, 2014). To validate the use of a direct Fourier filter, we compared the output trajectories with those obtained using Lanczos and Butterworth filters instead of Fourier, as they are known to be less subject to the Gibbs effect (Thomson & Emery, 2014). Results are shown for a threshold set at $1.25 \times 10^{-5} \cdot s^{-1}$ as in the rest of the study. The trajectories obtained are presented in Figure D1 for *Pierre-Henri*, *Peter*, and *Rose*. The results compare well for

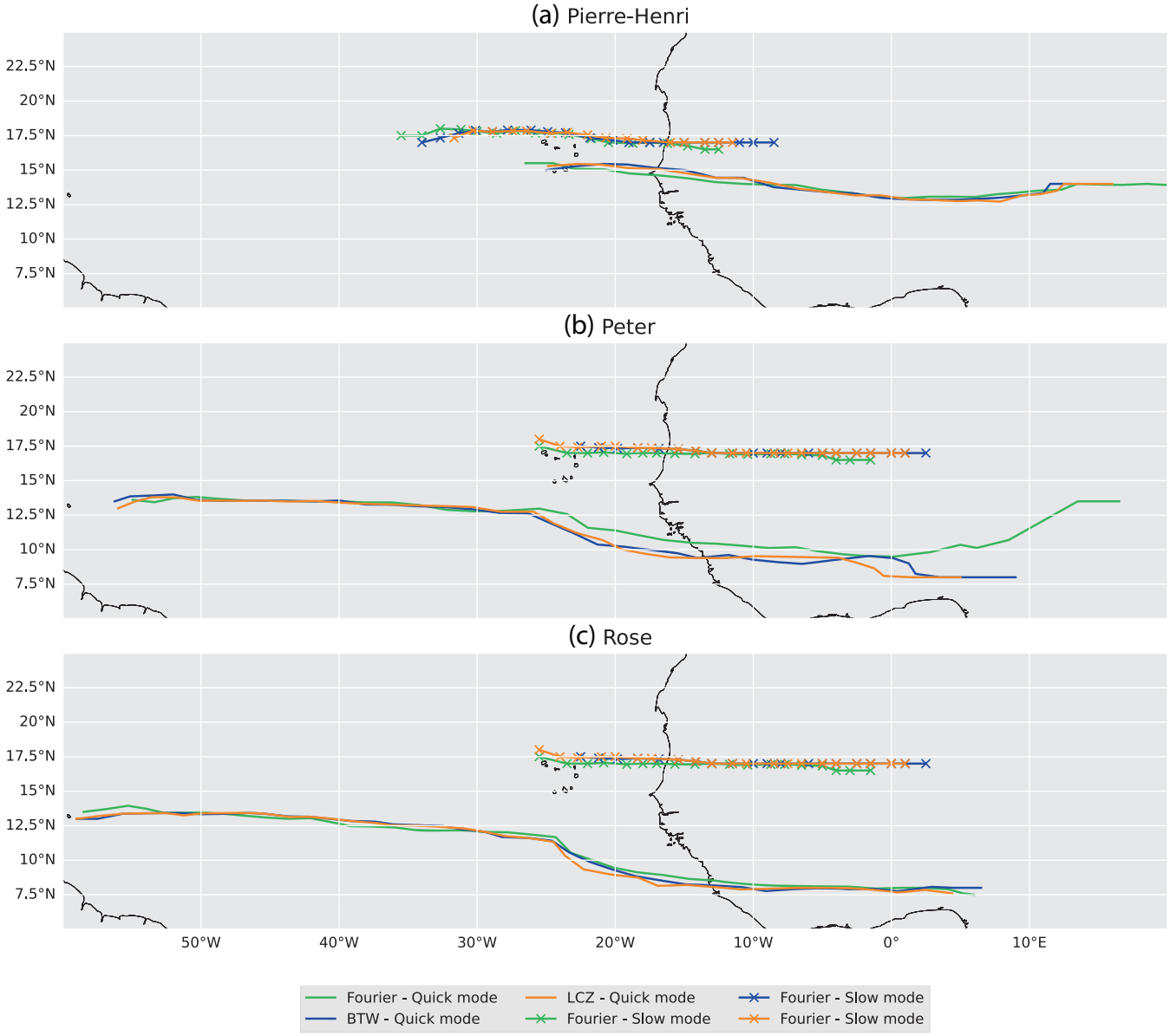

FIGURE D1 Comparison of trajectories derived from the automated tracking presented in this study using three band-pass filters (2–10 days, slow mode, and quick mode) and Jonville et al. (2024) tracking for the AEWs associated with (a) *Pierre-Henri*, (b) *Peter*, and (c) *Rose*. Trajectories derived from the manual track appear as dashed lines, whereas those derived from the automated tracking appear as solid lines. The trajectories derived with the 2–10 day band-pass filter are green. The trajectories associated with the quick and slow modes are in blue and orange, respectively.

all trajectories and modes, validating the use of the direct Fourier filter in these case studies.

APPENDIX E. SENSITIVITY ANALYSIS ON DISTANCE THRESHOLD FOR AEW–TC INTERACTION

The choice of the threshold for the maximum distance separating two objects considered as interacting is somehow arbitrary. To ensure that it does not impact our results, we conducted a sensitivity analysis on this threshold. The results for different values are presented in Table E1. The thresholds presented correspond to the following:

- 5×10^5 m: order of magnitude of the radius of a cyclone;
- 1×10^6 m: order of magnitude of the diameter of a cyclone;
- 1.5×10^6 m: half an AEW wavelength.

The trends presented in Section 4 are robust to the choice of threshold. Figure E1 shows the evolution of the

TABLE E1 TC matching: sensitivity to collision threshold.

Filtering modes	Matching wave track	Collision threshold		
		5×10^5 m	1×10^6 m	1.5×10^6 m
Mode 2–10 days	Any	56.6%	60.8%	67.0%
	North	14.1%	23.1%	40.6%
	South	47.2%	50.0%	51.4%
	North and south	4.7%	12.3%	25.0%
Quick mode (only)	Any	52.8%	58.5%	65.7%
	North	15.6%	22.64%	34.9%
	South	44.8%	49.52%	53.3%
	North and south	7.55%	13.67%	22.6%
Slow mode (only)	Any	21.7%	30.7%	42.5%
	North	16.0%	23.11%	33.5%
	South	7.54%	11.8%	15.1%
	North and south	1.89%	4.25%	6.13%
Quick and slow mode (combined)	Any	57.1%	63.7%	73.1%
	North	26.4%	37.3%	51.4%
	South	48.1%	53.3%	57.5%
	North and South	17.5%	26.9%	35.8%

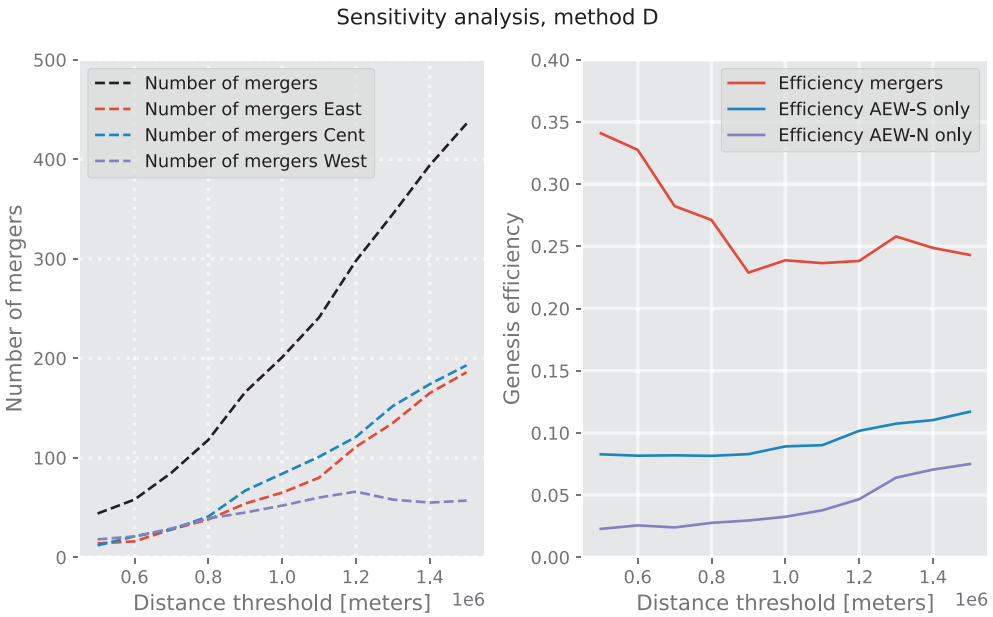

FIGURE E1 Evolution of the number of mergers detected, and of genesis efficiency when tracking with quick-mode ∪ slow-mode tracking as a function of the distance threshold chosen. In the left panel, East mergers are mergers detected east of 20°W, Cent(ral) mergers are mergers detected between 20°W and 40°W, and West mergers are mergers detected west of 40°W.

number of mergers detected and the genesis efficiencies from AEW-N, AEW-S, and mergers as a function of the distance threshold with quick-mode ∪ slow-mode tracking. Again, the results presented in Section 4 are sensitive to the threshold but qualitatively robust. The efficiency of mergers decreases when the threshold increases from 500 km to 800 km as the number of mergers increases. From 800 km onwards, it plateaus as the increase in the number of TC/merger matches increases with the threshold.